XCT-informed coupled creep-damage FE model for time-dependent micromechanical behavior of hardened cement pastes

Minfei Liang [a,b], Yong Fang[a*], Yidong Gan [c*], Wenqi Guo[a], Chuan He[a], Sonia Contera [b], Erik Schlangen [d], Branko Šavija [d]

[a] Key Laboratory of Transportation Tunnel Engineering, Ministry of Education, Southwest Jiaotong University, Chengdu, 610031, Sichuan, China
[b] Clarendon Laboratory, Department of Physics, University of Oxford, Oxford, OX1 3PU, UK
[c] School of Civil and Hydraulic Engineering, Huazhong University of Science and Technology, Wuhan, 430074, China.
[d] Microlab, Faculty of Civil Engineering and Geosciences, Delft University of Technology, Delft 2628CN, The Netherlands.

minfei.liang@physics.ox.ac.uk; ygan@hust.edu.cn; swjtuguowenqi@163.com; chuanhe21@swjtu.edu.cn; Sonia.AntoranzContera@physics.ox.ac.uk; Erik.Schlangen@tudelft.nl; B.Savija@tudelft.nl
*Corresponding author: fy980220@swjtu.cn; ygan@hust.edu.cn;

ABSTRACT
This study presents an experimentally informed coupled creep–damage modelling framework for the time-dependent micromechanical behaviour of hardened cement paste. Using realistic microstructures, a viscoelastic formulation solved by an exponential algorithm, and a continuum damage model, the framework consistently captures microscale creep, creep recovery, and strain-rate-dependent response. The results show that microstructural discretization strongly affects predictions: coarse discretizations underestimate porosity and overestimate hydration, leading to overpredicted stiffness and strength. The model reproduces measured flexural strength, elastic modulus, and the observed brittle failure. Low-stress creep and recovery are predicted accurately, with high recovery ratios indicating predominantly linear creep. The calibrated HD-CSH/ LD-CSH creep modulus ratio is consistent with experimental insights, supporting that calcium hydroxide increases the creep modulus of CSH. Strain-rate effects are also captured: slower loading allows more creep and earlier damage in weaker phases, while faster loading drives damage into stronger phases, yielding higher apparent stiffness and strength with more pronounced damage patterns. Overall, the framework provides a physically consistent basis for studying microscale creep–damage interactions. Future work will incorporate temperature and moisture effects and extend the approach to multiscale simulations of long-term concrete behavior under realistic environments.

Keywords: cement paste; creep; damage; microstructure; calcium-silicate-hydrate.

1 Introduction

Concrete creep is a time-dependent deformation that occurs under sustained loading and is widely recognized as a key phenomenon affecting the durability of concrete structures [1]. At early ages, creep—representing the viscoelastic behavior of concrete—is a critical input for quantifying stress relaxation caused by restrained shrinkage, which directly governs the risk of early-age cracking [2–4]. Over longer time scales, creep may result in excessive deformation and the loss of prestress in concrete members [5–7]. Consequently, accurate prediction of concrete creep is essential for ensuring the serviceability and durability of concrete structures.

As a composite of cement paste and aggregates, concrete can often be analyzed at different scales with focuses on different phases and mechanisms [8,9] (**Fig.1**). The aggregates, often made of natural stones and sands that have dense microstructures, are mostly considered as the elastic phases that do not creep [10]. The cement paste, primarily composed of C-S-H gels, pores, and clinkers, has been recognized as the main creeping phase [11]. The major factors governing the effective creep of the cement paste are often attributed to the viscoelastic property, volume, morphology, and structural arrangement of the C-S-H gels [12,13], induced by micromechanical processes such as solidification and microprestress [14], microcracking [15], hydration [16], etc. Therefore, a good understanding and characterization of the microstructure is an essential step for predicting the creep behavior of cement paste and concrete.

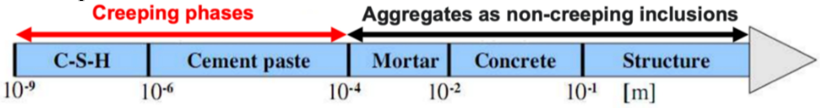

Fig.1 Multiscale perspective of concrete materials and structures

Models for predicting microscale creep behavior can generally be classified into three categories: micromechanical homogenization (MH), continuous finite element (CFE), and discrete finite element (DFE). By performing classical micromechanical homogenization methods such as Mori–Tanaka and Self-Consistent schemes in the Laplacian domain, MH directly predicts the effective viscoelastic properties using the volume fractions and intrinsic properties of hydration products as inputs [11,17–19], which can be obtained from micro-indentation tests [20–22] or, alternatively, identified by downscaling macroscopic creep measurements through a similar micromechanical framework [23]. A multiscale benchmark across different homogenization schemes and constituent assumptions has further validated this approach [24].

Unlike MH, which embeds implicit morphological assumptions in its analytical expressions, the CFE approach explicitly represents the microstructure and evaluates the corresponding viscoelastic response using linear viscoelastic models such as Maxwell or Kelvin chains [12,25,26]. Both MH- and CFE-based studies have been validated against micro-indentation or macroscale creep experiments, representing notable advances in this field. Despite this progress, several limitations remain. Most MH and CFE methods rely on simplified assumptions regarding the morphology and spatial arrangement of microstructural phases, which can strongly influence the resulting viscoelastic behavior [16]. Moreover, these approaches typically assume a linear viscoelastic regime and therefore cannot capture damage-induced nonlinearity under different stress levels.

In recent years, the DFE approach has been increasingly used to characterize the micromechanical properties of cement paste by employing realistic microstructural inputs. Based on microstructures obtained from Backscattered Electron (BSE) microscopy and X-ray Computed Tomography (XCT), the Lattice Fracture Model (LFM) [27,28], a representative DFE method, has been successfully applied to predict compressive strength [29], tensile strength [30], flexural strength [31], fatigue behavior [32], and other mechanical properties. Parallel to these modelling efforts, corresponding micromechanical testing techniques have been developed: micro-specimens can be fabricated using a micro-dicing saw and subsequently tested in a nanoindentation device to obtain micromechanical behavior and properties. These measurements provide essential reference data for developing and validating micromechanical models of cementitious materials [29,33].

DFE-based methods have also been applied to investigate the short-term creep behavior of cement paste at the microscale. Short-term creep measurements on cantilever beams fabricated from ordinary Portland cement and high-volume slag cement have been reported [34]. The effects of water-to-cement ratio and strain rate on creep compliance and creep recovery have also been examined [35,36]. Using the local force method, an LFM-based framework was further developed to simulate microstructural effects on short-term creep [37], and the results demonstrated good agreement with experimental observations. Compared with MH and CFE methods, LFM directly incorporates realistic microstructural features and implicitly accounts for damage evolution during creep by removing damaged lattice elements at each computation step. However, local force -based implementations of LFM are limited to short-term creep under constant loading. A recent extension introduced direct stress integration based on the Volterra integral to enable simulations under varying load histories [38]. Nevertheless, direct implementation of the integral requires storing all internal variables of the rheological chains at every computational step, which leads to substantial computational cost and memory demand, posing challenges for efficiency and scalability [39].

In summary, current microscale modelling frameworks for cement paste creep often face three key challenges: (1) accurately representing realistic microstructures; (2) efficiently performing stress/strain integration within the Volterra integral, which is computationally demanding; and (3) incorporating damage evolution to capture nonlinear creep under different stress levels. To address these limitations, this study proposes a coupled creep-damage modelling framework that integrates an exponential algorithm for efficient numerical stress and strain integration with a continues damage model. The framework takes experimentally measured microstructures and micromechanical properties as input and is evaluated using a comprehensive series of microscale cantilever beam tests.

The remainder of this paper is organized as follows. Section 2 presents an overview of the microscale cantilever beam experiments, including short- term creep, creep recovery, and micromechanical characterization under different strain rates. Section 3 introduces the theoretical formulation and material subroutine. Section 4 provides detailed implementation of the proposed coupled creep–damage numerical framework. Section 5 compares the numerical predictions with the experimental results to validate the accuracy and robustness of the proposed modelling approach.

2 Experimental Overview

This section presents a brief overview on the micromechanical tests of the miniaturized cantilever beams (MCBs) (**Fig.2**), which will be used as the input of the proposed models and provide ground truth for model validation. Details of these tests can be found in [34–36].

2.1 Sample Fabrication

The MCBs were fabricated from hardened cement paste to enable micromechanical characterization (**Fig.2a left**). Paste cylinders were first prepared using a standard CEM I 42.5N Portland cement (ENCI, the Netherlands) with a Blaine fineness of 284 m^2/kg, and deionized water, mixed at w/c ratios of 0.30, 0.40, and 0.50. To mitigate bleeding at higher w/c, the freshly cast cylinders were rotated at 2.5 rpm for 24 h at 26 °C during the initial setting period. The samples were then cured for 28 days under sealed conditions and room temperature (26 °C). Hydration was subsequently arrested via isopropanol solvent exchange. The cured paste was sliced into 3-mm plates, grounded and polished to obtain parallel and smooth surfaces, and then processed using a precision micro-dicing saw. Following two orthogonal cutting passes with controlled spacing, arrays of beams with a nominal geometry of 300 μm × 300 μm in cross-section and 1.65 mm in length were produced. ESEM imaging confirmed dimensional accuracy within ±1.5–2 μm and the absence of machining-induced damage (**Fig.2a right**).

2.2 Micromechanical Testing

All micromechanical bending tests were conducted using a KLA G200 nanoindenter equipped with a diamond cylindrical wedge tip, which applied a vertical line load to the free end of each MCB (**Fig.2b left**). The cement-paste mother plate (holding the MCB array at its fixed end) was bonded to a rigid metal baseplate using cyanoacrylate adhesive, and precise alignment of the loading tip with the beam axis was achieved under the in-situ optical microscope. Tests were performed in a thermally insulated chamber, with temperature and relative humidity maintained within narrow ranges (26.3 ± 0.4 °C and 34.2 ±0.8%) to avoid significant thermal drift and moisture exchange during loading.

It should be noted that drying has a negligible influence on the measured creep response. During the 28 days of sealed curing, hydration progressively consumed pore water; the resulting self-desiccation reduced the internal RH below 100 %, with associated autogenous shrinkage. The subsequent isopropanol solvent exchange replaced the residual pore water. By the time of testing, the MCBs are close to moisture equilibrium with the laboratory environment, owing to the extremely thin cross-section with a volume-to-surface ratio of only 0.07 mm; companion-MCB weight measurements during the short-term creep tests further confirm that almost no weight loss occurs. Given the short loading duration (≤ 1500 s), the autogenous shrinkage during the test can also be neglected, and the measured response is therefore interpreted as the basic creep of pre-dried cement paste rather than as drying creep in the Pickett-effect sense.

Prior to each experiment, the system drift rate was verified to be below 0.05 nm/s, and reference tests on glass MCBs were used to quantify the intrinsic instrumental drift. Measured displacements were corrected for baseplate and adhesive-layer deformation contributions, which were quantified by finite-element modelling of the test set-up as 14 % and 0.5 % of the total tip displacement, respectively [34,40]; these contributions are subtracted from the recorded displacement before converting it to beam curvature and strain. The detailed microstructures of MCBs with w/c ratios of 0.30, 0.40, and 0.50 were captured using XCT (**Fig.2b right**). Scans were performed at 90 kV and

170 µA with a voxel size of approximately 1.1 µm (voxel volume ~1.3 µm³), enabling identification of the main cementitious micro-phases. These microstructures will be used as the input of the subsequent modelling tasks.

2.3 Loading Schemes

Three loading schemes were employed to characterize the time-dependent micromechanical behavior of the micro-cantilever beams:

1) Short-term creep tests were performed under load control by rapidly loading each beam to the target stress level within 5s—30% of its flexural strength—and then maintaining the load for 800 s (**Fig. 2c, left**). The measured time-dependent deflection was converted into creep strain and creep compliance using classical cantilever beam theory.
2) To assess the recoverability of viscoelastic deformation, creep recovery tests adopted the same initial loading–holding sequence, followed by a controlled unloading to 1% residual load and a second holding stage (**Fig. 2c, middle**). The durations of the first and second holding stages were 180 s and 600 s, respectively.
3) Strain-rate–dependent bending tests were conducted to examine the rate sensitivity of stiffness and strength. MCBs were monotonically loaded until failure at strain rates ranging from approximately 10^{-6}/s to 10^{-2}/s (**Fig. 2c, right**).

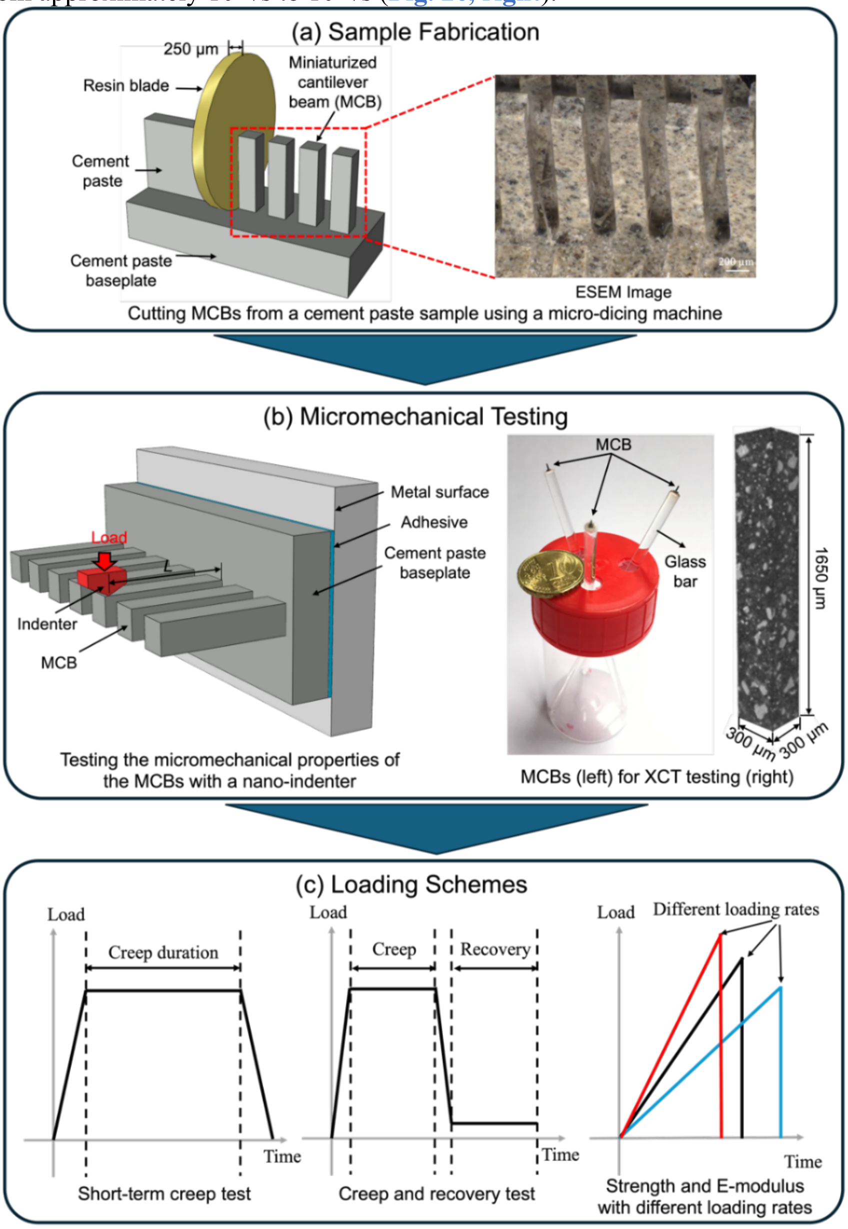

Fig. 2 Overview of the micromechanical bending tests on MCB specimens

(adapted from [34–36])

3 Coupled Creep-Damage Model

To describe the time- and rate- dependent behavior of the cement paste at the microscale, this study proposes a constitutive model that combines viscoelastic creep, tensile/ compressive damage mechanics, and simple rate-dependent viscoelasticity within a unified framework.

3.1 Viscoelastic Creep

This section first presents the viscoelastic creep formulation and the exponential algorithm [39,41,42], which will then be coupled with the damage model. Following the Boltzmann superposition and considering viscoelasticity, the strain can be expressed by the Volterra integral:

$$\varepsilon(t) = \int_0^t J(t-t')\, d\sigma(t') \tag{1}$$

where J is the creep compliance; t is the current time; t' is the time when load is applied. Note that herein the aging of material properties is not considered and therefore J is only the function of the loading duration $(t-t')$. Assuming a linear variation over each time increment $[t_i,\ t_{i+1}]$, Eq. (1) can be rewritten in the incremental form:

$$\Delta\sigma = E^*(\Delta\varepsilon - \Delta\varepsilon^{cr}) \tag{2a}$$

with the effective modulus E^*:

$$E^* = \frac{\Delta t}{\int_{t_i}^{t_{i+1}} J(t_{i+1}-t')dt'} \tag{2b}$$

and the incremental creep strain $\Delta\varepsilon^{cr}$:

$$\Delta\varepsilon^{cr} = \int_0^{t_i} [J(t_{i+1}-t') - J(t_i-t')]\dot{\sigma} dt' \tag{2c}$$

Eq. (2c) shows that computing $\Delta\varepsilon^{cr}$ requires storing and revisiting the entire stress history, which becomes computationally demanding for fine meshes or complex microstructures [38]. To avoid this costly convolution, the exponential algorithm approximates the creep compliance J by a Dirichlet series corresponding to an N-unit Kelvin chain:

$$J(t-t') = \frac{1}{E_0(t')} + \sum_{j=1}^{N} \frac{1}{E_j(t')}(1 - e^{-\frac{t-t'}{\mu_j}}) \tag{3}$$

where E_j and μ_j denote the elastic modulus and retardation time of the j-th Kelvin element. Note that the Kelvin-chain representation also admits a micromechanical interpretation, where each Kelvin unit can be associated with solid-matter sliding along a viscous nanoscale interface within the cement paste [43,44].

Substituting Eq. (3) into Eq. (2b, 2c), and evaluating the integrals using the midpoint rule under the assumption of linear stress variation during $[t_i,\ t_{i+1}]$, yields closed-form expressions for the effective creep modulus and incremental creep strain [39,45]:

$$E^*(t^*) = \frac{1}{\frac{1}{E_0(t^*)} + \sum_{j=1}^{N} \frac{1}{E_j(t^*)}(1 - (1 - e^{-\frac{\Delta t}{\mu_j}})\frac{\mu_j}{\Delta t})} \tag{4a}$$

$$\Delta\varepsilon^{cr} = \sum_{j=1}^{N} (1 - e^{-\frac{\Delta t}{\mu_j}})\, \varepsilon_j^*(t_i) \tag{4b}$$

where the hereditary internal variables of the Kelvin chain obey:

$$\varepsilon_j^*(t_{i+1}) = e^{-\frac{\Delta t}{\mu_j}} \varepsilon_j^*(t_i) + \frac{1}{E_j(t^*)}(1 - e^{-\frac{\Delta t}{\mu_j}})\frac{\mu_j}{\Delta t}\Delta\sigma \tag{4c}$$

A key advantage of this formulation is that the history term becomes entirely expressible in terms of the internal variables ε_j^* for each Kelvin unit. These variables can be updated recursively using Eq. (4c), eliminating the need for storing or integrating the full stress history required by Eq. (2c). Consequently, the viscoelastic evolution reduces to a sequence of quasi-elastic incremental problems, offering both computational efficiency and numerical stability.

3.2 Tensile/ Compressive Damage

This section introduces the constitutive damage formulation based on continuum damage mechanics, which will subsequently be coupled with the viscoelastic creep model described in Section 3.1. According to the Mazars damage model [46], the stress–strain relation of quasi-brittle solids subjected to stiffness degradation can be expressed as:

$$\sigma = (1-d)C_0\varepsilon \tag{5}$$

where $d \in [0,1)$ is the scalar damage variable and C_0 is the undamaged elastic stiffness tensor. Taking the rate form of Eq. (5) yields:

$$\dot{\sigma} = (1-d)C_0(\dot{\varepsilon} - \frac{\dot{d}}{1-d}\varepsilon) \tag{6}$$

where the second term inside the parentheses represents the strain contribution associated with damage evolution. Damage initiation and evolution are governed by a loading function that depends on the equivalent strain ε_{eq} and an initial threshold strain ε_0:

$$f(\varepsilon_{eq}, \varepsilon_0) = \varepsilon_{eq} - \varepsilon_0(d) = 0 \tag{7}$$

Before the onset of damage, the threshold strain is defined as:

$$\varepsilon_0(d=0) = \frac{f_{ct}}{E_0} \tag{8}$$

where f_{ct} is the tensile strength and E_0 is the undamaged elastic modulus. Once $\varepsilon_{\mathrm{eq}}$ exceeds ε_0, the threshold strain is updated to the current value of $\varepsilon_{\mathrm{eq}}$ to ensure irreversibility. Following the Mazars' formulation [46], the equivalent strain ε_{eq} is defined using the positive parts of the principal strains ε_i^{pr} $(i = 1, 2, 3)$:

$$\varepsilon_{eq} = \sqrt{\langle\varepsilon_1^{pr}\rangle_+^2 + \langle\varepsilon_2^{pr}\rangle_+^2 + \langle\varepsilon_3^{pr}\rangle_+^2} \tag{9}$$

where $\langle\cdot\rangle$ denotes the Macaulay brackets (e.g., $\langle x\rangle_+ = \max(x, 0)$). The maximum value of the equivalent strain ε_{eq} is recorded at each increment to ensure irreversibility. The damage evolution is computed as a weighted combination of the tensile damage d_t and compressive damage d_c:

$$d = \alpha_t d_t + \alpha_c d_c \tag{10}$$

where the tensile and compressive weights, α_t and α_c, depend on the contributions of positive and negative principal strains:

$$\alpha_t = \frac{\sum_{i=1}^{3}\langle\varepsilon_i^{pr}\rangle_+}{\sum_{i=1}^{3}(\langle\varepsilon_i^{pr}\rangle_+ + |\langle\varepsilon_i^{pr}\rangle_-|)}, \ \alpha_c = 1 - \alpha_t \tag{11}$$

The original Mazars' damage model [46] implemented an explicit expression for damage evolution and typically requires nonlocal or gradient regularization techniques to avoid mesh dependence [47]. To reduce computational complexity while maintaining objectivity, this study adopts a fracture-energy-based regularization using an exponential softening law (**Fig. 3(a)**) [48]:

$$d_t = 1 - \frac{\varepsilon_0}{\varepsilon_{eq}} e^{(\frac{\varepsilon_0 - \varepsilon_{eq}}{\varepsilon_{tu} - \varepsilon_0})} \tag{12a}$$

where the softening tensile strain ε_{tu} is related to the tensile fracture energy G_{ft} and characteristic length of the element h:

$$\varepsilon_{tu} = \varepsilon_0 + \frac{G_{ft}}{E_0\varepsilon_0 h} \tag{12b}$$

Compressive damage is described using the constitutive stress–strain relationship of concrete adopted in Model Code 2010 (MC2010) (**Fig. 3(b)**) [48,49]. Note that the mechanical response of considered experiments here (see section 2) is dominated by tensile damage, and compressive damage parameters are not yet calibrated in this study. The MC2010 formulation is therefore used only to complete the constitutive description and does not affect the main results. The evolution of compressive damage d_c is defined as

$$d_c = \begin{cases} 1 - \dfrac{(k\bar{\varepsilon}_{ceq} - \bar{\varepsilon}_{ceq}{}^2)f_{cm}}{\left(1 + \bar{\varepsilon}_{ceq}(k-2)\right)E_0\varepsilon_{ceq}} & if\ \varepsilon_{ceq} \le \varepsilon_{c1} \\ 1 - \dfrac{f_{cm}}{E_0\varepsilon_{ceq}} & if\ \varepsilon_{c1} < \varepsilon_{ceq} \le \varepsilon_{c2} \\ 1 + \dfrac{k_1}{E_0} - \dfrac{k_2}{E_0\varepsilon_{ceq}} & if\ \varepsilon_{c2} < \varepsilon_{ceq} \le \varepsilon_{cu} \end{cases} \tag{13a}$$

Here,

$$\varepsilon_{ceq} = \frac{\varepsilon_{eq}}{\sqrt{2}\nu};\ \bar{\varepsilon}_{ceq} = \frac{\varepsilon_{ceq}}{\varepsilon_{c1}};\ k = \frac{1.05E_0\varepsilon_{c1}}{f_{cm}};$$
$$k_1 = \frac{f_{cm}}{(\varepsilon_{cu} - \varepsilon_{c2})};\ k_2 = f_{cm} - k_1\varepsilon_{c2} \tag{13b}$$

where f_{cm} is the compressive strength; k, k_1, k_2 are the shape parameters of the constitutive curve; ε_{c1} and ε_{c2} are parameters adopted from MC2010. The equivalent ultimate compressive strain can be extrapolated by the compressive fracture energy G_{fc}:

$$\varepsilon_{cu} = \frac{2G_{fc}}{f_{cm}h} - (\varepsilon_{c2} - \varepsilon_{c1}) \tag{13c}$$

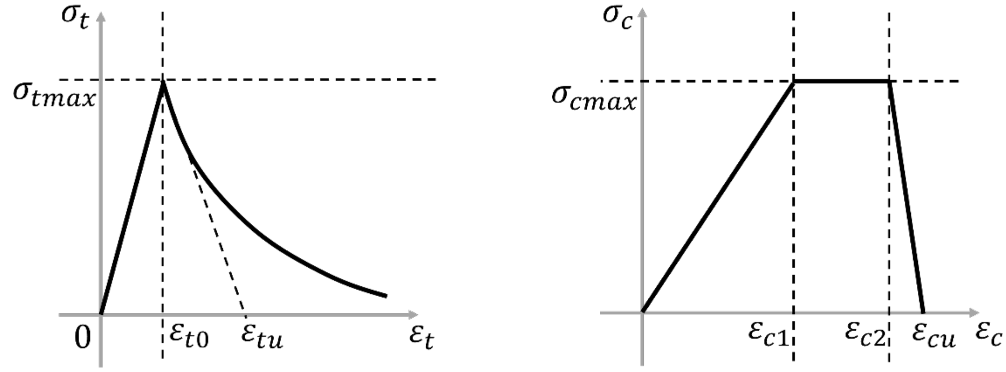

(a) (b)

Fig. 3 Tensile (a) and compressive (b) stress versus equivalent strain for the damage model

3.3 Coupling of Creep and Damage

Building upon the viscoelastic creep formulation in Section 3.1 and the damage formulation in Section 3.2, the proposed coupled creep–damage model adopts an incremental framework capable of capturing the mutual interactions between viscoelasticity, damage evolution, and irreversible viscous deformation. The incremental constitutive relation is expressed as:

$$\Delta\sigma = (1 - d)C_0\Delta\varepsilon^{el} \tag{14}$$

where $\Delta\varepsilon^{el}$ is the incremental elastic strain. Following the infinitesimal strain assumption, the incremental total strain $\Delta\varepsilon^{tot}$ can be decomposed as:

$$\Delta\varepsilon^{tot} = \Delta\varepsilon^{el} + \Delta\varepsilon^{cr} + \Delta\varepsilon^{dm} + \Delta\varepsilon^{irr} \tag{15}$$

where $\Delta\varepsilon^{cr}$, $\Delta\varepsilon^{dm}$, $\Delta\varepsilon^{irr}$are the incremental creep strain, damage strain, and irrecoverable strain induced by viscous flow, respectively. These strain components are coupled by the following mechanisms [45,50]:

1) The creep strain partly contributes to the equivalent strain ε_{eq} as defined in Eq. (9), which drives the damage evolution.
2) The damage induces the stiffness degradation during the creep process (Eq. (4a)).
3) Creep internal variables evolve under the damaged stress, affecting subsequent creep increments (Eq. (4c)).

3.3.1 Effective Strain for Damage Evolution

First, tentatively assuming viscoelastic creep and irreversible viscous flow do not directly contribute to microcrack formation, the damage evolution is driven by an effective elastic strain, defined as

$$\varepsilon^{eff} = \varepsilon^{tot} - \varepsilon^{cr} - \varepsilon^{irr} \tag{16}$$

Then, to capture the influence of time-dependent deformation on crack evolution, the effective strain is augmented by a creep-dependent term [45,50]:

$$\varepsilon_{\beta}^{eff} = \varepsilon^{eff} + \beta_{cr}\varepsilon^{cr} = \varepsilon^{tot} - (1 - \beta_{cr})\varepsilon^{cr} - \varepsilon^{irr} \tag{17}$$

where β_{cr} is a material parameter controlling the contribution of accumulated creep strain to the damage-driving strain measure, which requires calibration from nonlinear creep tests [50]. The augmented effective strain $\varepsilon_{\beta}^{eff}$ is used to compute the principal strains ε_i^{pr} and the equivalent strains ε_{eq} via Eq. (9), which in turn results in damage progression as defined in Eq. (10-13). Note that, as an alternative, the damage rate can be taken proportional to the strain rate with a proportionality factor increasing with the stress-to-strength ratio [51]. The present coupling instead uses a single continuum parameter at the microscale.

3.3.2 Creep Under Degrading Stiffness and Damaged Stress

The damage results in the stiffness degradation which accelerates the creep process. The effective modulus of the Kelvin Chain (Eq. (4a)) therefore needs to incorporate the damage factor:

$$E_{eff}^*(t^*) = (1-d)E^*(t^*) \tag{18}$$

The update of the hereditary internal variables of the Kelvin chain (Eq.(4c)) also needs to incorporate the stiffness degradation and contribution of the incremental stress induced by the damage $\Delta\sigma^{dm}$ and irreversible viscous strains $\Delta\sigma^{dm}$:

$$\varepsilon_j^*(t_{i+1}) = e^{-\frac{\Delta t}{\mu_j}}\varepsilon_j^*(t_i) + \frac{1}{(1-d)E_j(t^*)}\left(1-e^{-\frac{\Delta t}{\mu_j}}\right)\frac{\mu_j}{\Delta t}\left(\Delta\sigma - \Delta\sigma^{dm} - \Delta\sigma^{irr}\right) \tag{19}$$

Here,

$$\Delta\sigma^{dm} = C_{eff}^*:\Delta\varepsilon^{dm}, \quad \Delta\sigma^{irr} = C_{eff}^*:\Delta\varepsilon^{irr}, \tag{20}$$

in which the C_{eff}^* is the effective stiffness tensor assembled by the effective stiffness modulus E_{eff}^* from the Eq. (18). Then, $\Delta\varepsilon^{cr}$ can be updated for the next step according to Eq.(4b).

3.3.3 Irreversible Viscous Flow

To simulate the irreversible viscous flow of the cementitious material consistent with the solidification theory [52], an irreversible viscous flow term is included. A simple overstress-type viscoplastic law governs this strain component [45]:

$$\Delta\varepsilon^{irr} = \frac{\langle|\sigma| - \sigma_y\rangle_+}{\eta_p} sign(\sigma)\Delta t \tag{21}$$

where σ_y is the tensile or compressive yield threshold, expressed as a fraction of the corresponding strength, and η_p is the viscosity parameter. The operator sign(σ) ensures that the irreversible strain develops in the same direction as the applied stress—i.e., positive in tension and negative in compression. This term will contribute to stress update but does not influence the creep internal variables and damage update.

3.3.4 Stress Update

By substituting Eq. (15) into Eq. (14) and replacing the stiffness tensor with C_{eff}^*, the stress update expression is obtained:

$$\Delta\sigma = C_{eff}^*(\Delta\varepsilon^{tot} - \Delta\varepsilon^{cr} - \Delta\varepsilon^{dm} - \Delta\varepsilon^{irr}) \tag{22}$$

where $\Delta\varepsilon^{cr}$ and $\Delta\varepsilon^{irr}$ are computed according to section 3.3.2 and 3.3.3, respectively. The incremental damage strain $\Delta\varepsilon^{dm}$ is derived from Eq. (6) using the effective strain:

$$\Delta\varepsilon^{dm} = \frac{\dot{d}}{1-d}\varepsilon^{eff} \tag{23}$$

3.4 Material subroutine

The coupled creep–damage constitutive framework is implemented in ABAQUS through a user-defined material subroutine (UMAT) written in Fortran, in which all viscoelastic, damage, and irreversible viscous mechanisms are evaluated incrementally at each integration point. The algorithmic sequence of the UMAT is summarized in **Fig. 4**.

At the beginning of each increment, the UMAT retrieves the state variables from the previous step—including the Kelvin-chain hereditary strains, accumulated creep strain, irreversible viscous strain, and tensile/compressive damage history—together with the strain increment prescribed by the finite element solver. Using these variables, the UMAT first computes the effective modulus and the creep strain increment via the exponential algorithm of Eq. (4), after which the irreversible viscous strain is evaluated according to the overstress-based viscoplastic formulation in Eq. (21). These contributions are used to construct the effective strain measures defined in Eq. (16-17), enabling the computation of principal effective strains and the equivalent strain that governs tensile and compressive damage evolution following Eq. (7-13). The resulting damage variable degrades the elastic stiffness and directly influences both the stress response and the subsequent creep development. After the damage variable is updated, the UMAT evaluates the stress increment using the coupled relation in Eq. (21), accounting simultaneously for elastic, creep, damage, and irreversible viscous components. The stress obtained at the end of the increment is then used to update the hereditary internal variables of the Kelvin chain according to Eq. (19), ensuring that the material retains full memory of the viscoelastic deformation history. All updated internal variables are stored back into the UMAT state-variable array to be used in the next increment.

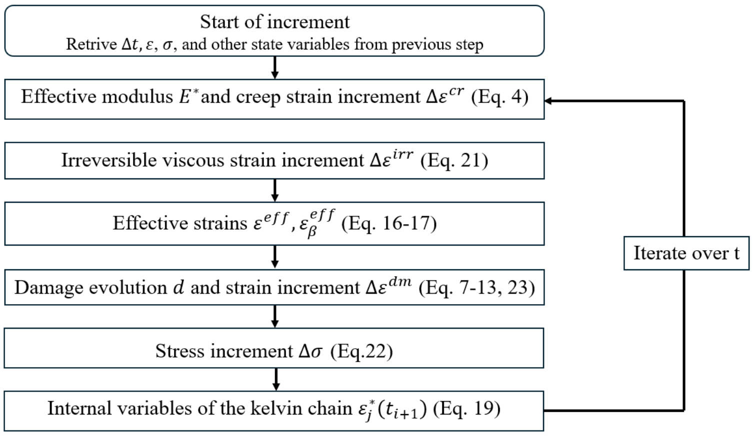

Fig. 4 The material subroutine of the coupled creep-damage model

4 Implementation

This section describes the segmentation of the microstructural images for generating the multiphase input for the FE model. The procedure used to identify and separate the individual material phases is first presented, followed by a discussion of the material properties assigned to each phase. Finally, the overall configuration of the FE model, including geometric representation, mesh characteristics, loading and boundary conditions, is introduced.

4.1 Multiphase segmentation

The microstructure of the MCBs with three different w/c ratios (0.30, 0.40, and 0.50) were obtained by XCT as described in section 2.2, which can then be used as the input of the coupled creep-damage model. The microstructure of the cement paste is then segmented into four different phases using threshold methods: pore, low-density calcium-silicate-hydrate (LD-CSH), high-density calcium-silicate-hydrate (HD-CSH), and unhydrated cement (UHC) [53–55]. The threshold values were calculated based on the PDF and CDF of the greyscale values of the XCT images (Fig. 5). The inflection point of the CDF is defined as the upper threshold value of the pore phase (S_1), which corresponds to the point where segmented pore areas start to overflow to surrounding paste [53]. Specifically, below this threshold the pore volume fraction increases gradually, whereas beyond it a small increment causes a disproportionate increase as CSH phases begin to be included as pores. The change of the tangent slope after the peak of the PDF is identified as the threshold value between HD-CSH and UHC (S_3) [56]. The threshold value between the LD- and HD-CSH (S_2) is identified based on the model proposed by Tennis and Jennings [57]:

$$M_r = 3.017\left(\frac{w}{c}\right)\alpha - 1.347\alpha + 0.538 \qquad (24a)$$

where M_r is the ratio of the mass of LD-CSH to HD-CSH; α is the hydration degree. The hydration degree can be estimated by the following equation:

$$\alpha = \frac{\frac{V_h}{V}}{\frac{V_h}{V} + V_u} \qquad (24b)$$

where V_h, V_u are volume fraction of hydration product and unhydrated particle respectively; V is the volume ratio of reaction product to reactant, which can be assumed as 2.2 according to [58]. This value corresponds to the overall hydration reaction of ordinary Portland cement and may require adjustment for cement with significantly different mineralogical compositions.

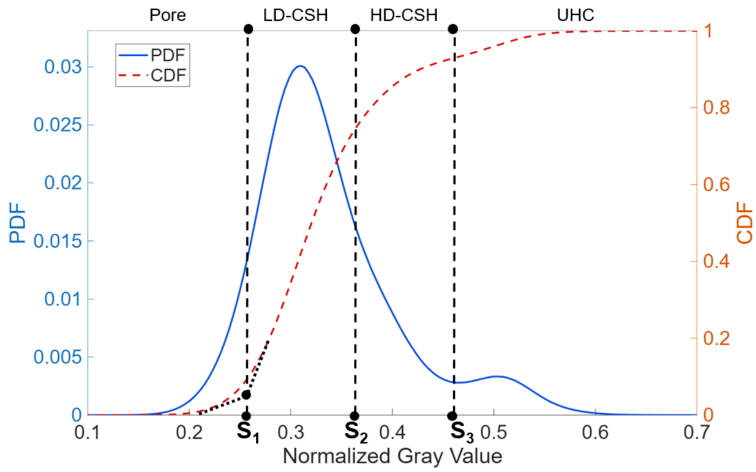

Fig. 5 The grey scale values of the XCT images of the cement paste sample w/c =0.50

It should be noted that the Tennis–Jennings model presumes two discrete LD- and HD-CSH phases. Recent ^{1}H NMR studies have shown, in contrast, that the density of C-S-H evolves continuously with the precipitation degree [59–62]; consistently, the grayscale histogram in **Fig. 5** is itself continuous and mono-modal. A binary LD/HD partition is nevertheless retained here as a pragmatic FE-input simplification, which is consistent with grid nanoindentation analyses that statistically identify two mechanical clusters of C-S-H [55] and is quantitatively prescribed by the Tennis–Jennings model [57] used above. A sensitivity study on the LD/HD threshold S2 is provided in Appendix A. Future work may pursue continuous, pixel-wise quantification of C-S-H mechanical properties directly from microstructure images using deep-learning techniques [63], bypassing the discrete LD/HD simplification adopted here.

Examples of the segmented microstructures are shown in **Fig. 6**. At low w/c, the hydration products are dominated by HD-CSH (**Fig. 6(a)**), whereas at high w/c, LD-CSH becomes the prevailing phase (**Fig. 6(c)**). The microstructure at the intermediate w/c contains comparable proportions of LD-CSH and HD-CSH (**Fig. 6(b)**). HD-CSH appears either as a dense rim surrounding unhydrated cement particles or as sparsely distributed clusters within the LD-CSH matrix; the latter is likely associated with calcium hydroxide (CH), which commonly forms in water-filled spaces and mixes with LD-CSH [56]. In general, increasing the w/c ratio leads to more hydration products (i.e., a higher degree of hydration) but also more porosity, and tends to produce larger amounts of LD-CSH relative to lower w/c mixtures [57].

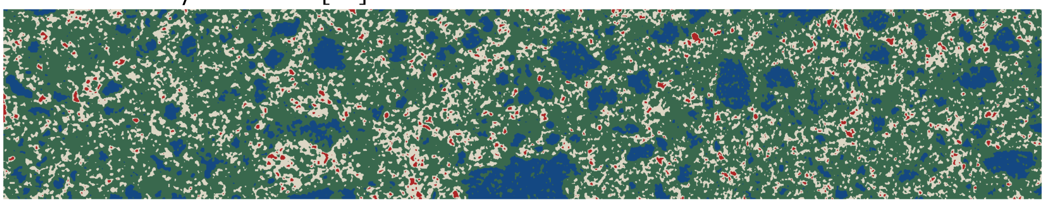

(a) w/c=0.30

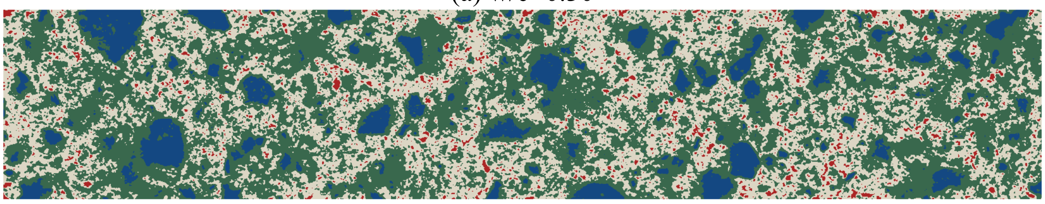

(b) w/c=0.40

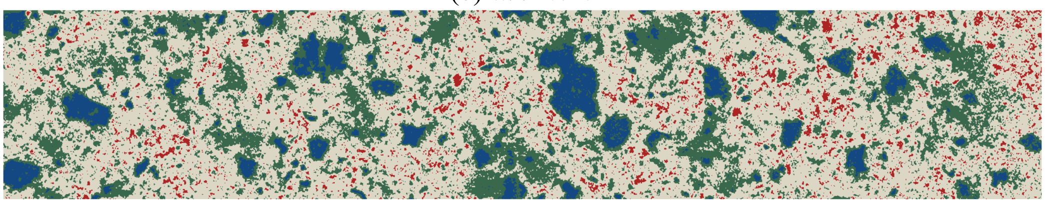

(c) w/c=0.50

(d) legend

Fig. 6 Segmented microstructures: (a~c) corresponds to w/c ratios ranging from 0.30, 0.40, to 0.50; **(d)** legend of each phase

4.2 Phase properties and identification

The material properties of LD-CSH, HD-CSH, and UHC are listed in **Table.1**. The identification of the material parameters refers to experimental literature on the micromechanical properties of cement paste. These literatures provide a limited range of these parameters and then the exact values used herein were calibrated further using the experimental results of the sample with $w/c = 0.30$. Detailed calibration procedures and discussions can be found in section 5.

The values of elastic modulus can often be found in the experimental study of micromechanical properties of cement paste [64,65], in which a grid of nanoindentation tests were conducted and therefore the mechanical properties of each micro phase can be statistically identified by Gaussian Mixture Model or Clustering methods [55,64,66]. However, it should be noted that the phase identified in the nanoindentation tests and XCT images might be different due to different testing resolution: the nanoindentation is testing an area relating to its indentation depth [67], while the XCT has a limited resolution (1.0 μm^3 herein). This study adopts elastic moduli obtained through a combined nanoindentation–XCT approach, where a linear relationship between indentation modulus and XCT attenuation coefficient was experimentally established and validated [68,69].

The tensile strengths of the CSH phases were determined with reference to mechanically compacted CSH strength tests [70], where the tensile capacity of CSH foam exceeded 24 MPa in the presence of micro-defects. A tensile strength of 40 MPa was assigned to LD-CSH after calibration against the w/c=0.30 experimental results [34]. Because the strength is known to scale linearly with nanoindentation hardness [71], the strength ratio between HD-CSH and LD-CSH can be inferred from the ratio between their hardness and therefore a value of 1.63 was adopted herein [72]. The compressive-to-tensile strength ratio of 8.0 follows micromechanical modelling of CSH [73]. The tensile and compressive fracture energy densities were assumed based on molecular dynamics simulations of crack nucleation and propagation in CSH at the atomic scale [74–76], and as a surface energy density, the fracture energy is expected to be relatively scale-insensitive over the nanometer-to-micrometer range considered here. The strain parameters governing the compressive damage curves (ε_{c1} and ε_{c2}) follow the MC2010 [42].

Table. 1 Material properties of each phase

	LD-CSH	HD-CSH	UHC
$E_0/\ GPa$	12	24	72
ν	0.2	0.2	0.2
$f_{ctm}/\ MPa$	40	65	150
$f_{cm}/\ MPa$	320	520	1230
$G_{fIt}/\ J/m^2$	0.5	1	5
$G_{fIc}/\ J/m^2$	10	20	100
ε_{c1}	0.0022	0.0022	0.0022
ε_{c2}	0.0035	0.0035	0.0035
$E_{cr}/\ GPa$	700	3000	10000
β_{cr}	0.1	0.1	0.1
σ_y	0.8	0.8	0.8
$\eta_p/\ GPa \cdot s$	170	820	10000

The parameters of creep process (E_{cr}, β_{cr}) and irreversible viscous process (σ_y, η_p) are calibrated using the experimental results of creep recovery of the sample with w/c =0.30. The creep compliance function $J(t-t')$ is defined by:

$$J(t-t') = \frac{1}{E_0} + \frac{1}{E_{cr}} f(t-t') \qquad (25)$$

where E_{cr} is the creep modulus; $f(t-t')$ is the function of the creep evolution, typically described by power or logarithmic trends [20,77,78]. The objective is to find the Kelvin chain that corresponds to the experimental results. Then, the Kelvin chain units (E_j and μ_j) can be used for the FEM analysis. Directly fitting the experimental results (Eq. 25) to the Dirichlet series of Kelvin chain (Eq. 3) can lead to non-unique solutions [79]. To avoid this ill-posedness, a nine-unit Kelvin chain was adopted, and its retardation times were prescribed a priori as

$$\mu_j = 10^{-6+j}, j = 1{:}9 \tag{26}$$

Considering the continuous retardation spectrum of the Kelvin chain, the creep evolution function can be expressed as

$$f(t-t') = \int_0^\infty \frac{1}{E_j}(1-e^{-\frac{t-t'}{\mu_j}})\, d(ln\,\mu_j) \tag{27}$$

from which the discrete Kelvin-chain moduli E_j can be computed using the Laplace-transform–based Widder formula [80]:

$$\frac{1}{E_j} = -ln10 * \lim_{k\to\infty} \frac{(-k\mu)^k}{(k-1)!} f^{(k)}(k\mu) \tag{28}$$

The functional form of f, along with the order of the retardation spectrum k. In this study, an order of 3 is used which is sufficient to represent the creep function.

4.3 FE configuration

The finite element modelling aims to simulate the micromechanical response of MCB under a plane-stress assumption. The computational domain is a 1650×300 μm² rectangle consistent with the specimen geometry. For each w/c, the 3D XCT volume is first segmented into four phases (pore, LD-CSH, HD-CSH, UHC), and multiple depth slices are randomly extracted to capture microstructural variability. Each slice serves as an independent 2D microstructural input, and the FE results will be averaged to obtain representative behavior.

A structured quadrilateral mesh of linear plane-stress elements with reduced integration (CPS4R) is employed. For a given mesh size, the segmented 2D microstructure is rescaled to the same resolution using a nearest-neighbor scheme, enabling a direct correspondence between phase information and finite element discretization. It should be noted that nearest-neighbor rescaling might introduce staircase-shaped phase boundaries if large mesh size is used. The mesh size is treated as a modelling hyper-parameter: coarse meshes reduce computational cost but may fail to resolve the fine microstructural morphology, whereas finer meshes preserve more microstructural detail at higher computational expense. Four mesh sizes—1.0, 2.0, 5.0, and 10.0 μm—are examined. Notably, the 1.0 μm mesh matches the voxel resolution of the XCT dataset and therefore represents the microstructure without information loss; the larger mesh sizes introduce controlled homogenization suitable for sensitivity analysis. Examples of the microstructures at $w/c = 0.30$ are shown in **Fig. 7**. All phases are modelled using the coupled creep–damage constitutive framework described in Section 3, with phase-specific parameters listed in **Table 1**.

The boundary conditions follow a classical cantilever configuration: the left edge is fully constrained, while the right end is subjected to a prescribed downward load. The loading history is applied in accordance with the experimental protocol shown in **Fig. 2(c)**.

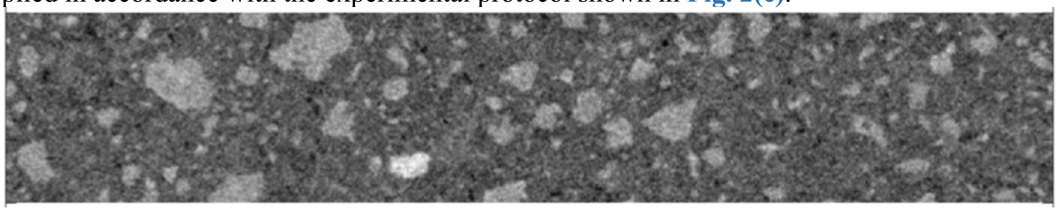

(a) original XCT image

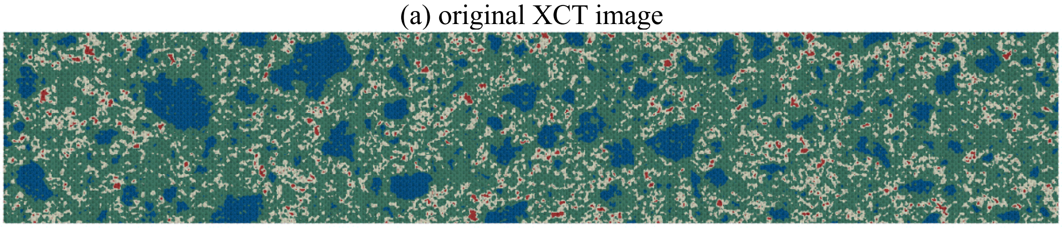

(b) mesh size =1.0 μm

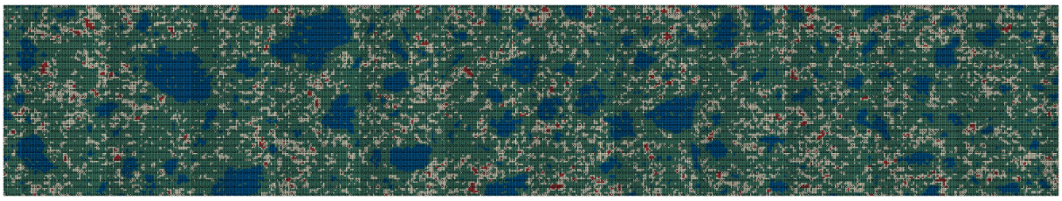

(c) mesh size =2.0 μm

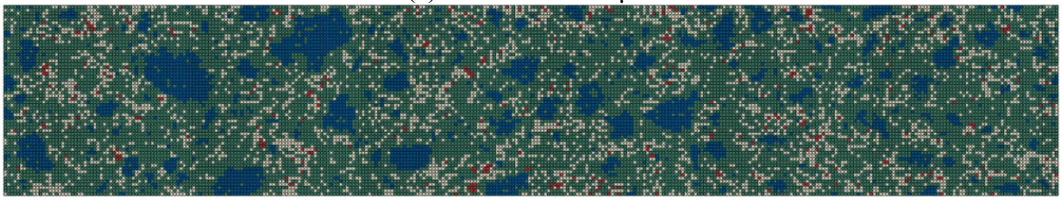

(d) mesh size =5 μm

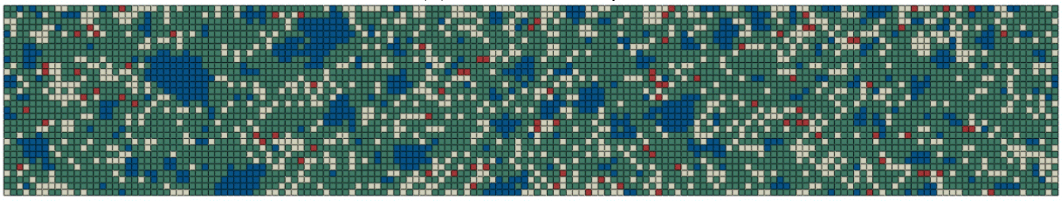

(e) mesh size =10 μm

(f) legend

Fig. 7 Microstructures of w/c 0.30 with different mesh size: (a) original microstructure **(b~e)** corresponds to mesh sizes ranging from 1.0, 2.5, 5.0, to 10.0 μm; **(f)** legend of each phase

5 Results and discussion

5.1 Creep function

Two types of creep functions, namely the power function $f_P(t-t')$ and the logarithmic function $f_L(t-t')$ [19,64,65], are compared here and expressed as

$$f_P(t-t') = \frac{1}{a}\left(\frac{t-t'}{t_{ref}}\right)^b \tag{29a}$$

$$f_L(t-t') = \frac{1}{a}\ln\left(b\left(\frac{t-t'}{t_{ref}}\right)+1\right) \tag{29b}$$

where a and b are fitting parameters; t_{ref} is a reference time introduced to render the time argument dimensionless ($t_{ref} = 1s$). Parameter a represents the composite-level creep modulus obtained from the bending test response, which differs from the phase-level creep moduli E_{cr} listed in Table 1. The fitting is performed using nonlinear least-squares regression implemented in the SciPy library [81], based on creep compliance data obtained from short-term creep tests on MCBs with three different w/c [30]. The fitting results are summarized in Fig. 8 and Table 2. The fitting accuracy is evaluated using the Root Mean Squared Error (RMSE) and the coefficient of determination (R^2).

The results indicate that both functions can adequately reproduce the experimental creep behavior, with R^2 values around or exceeding 0.99 for all cases. In previous studies on microindentation creep of CSH [20,82,83], the logarithmic function has been widely adopted to characterize creep evolution, as it was considered more suitable for representing long-term creep behavior. Moreover, these studies concluded that the fitting parameter b is independent of material composition and can be treated as a constant. Under this assumption, the creep function depends only on the parameter a, i.e., the creep modulus, implying that the creep behavior of C–S–H can be fully characterized by a single parameter. However, the fitting results obtained in the present study (Table 2) reveal different patterns:

- The power function consistently outperforms the logarithmic function, particularly when evaluated using RMSE. This observation is consistent with the established understanding that power-law behavior dominates short-term creep of cementitious materials, while logarithmic creep becomes relevant at longer timescales [84,85]. The present micro-cantilever results thus confirm this behavior at the microscale.

- For the logarithmic function, the parameter b exhibits a non-negligible variation, ranging from 0.024 to 0.072, corresponding to an almost 300% difference. In contrast, the parameter b in the power function varies from 0.333 to 0.430, showing a much smaller variation of approximately 30%. Assuming the parameter b is a constant, the power function can well describe the creep behavior of cement pastes with different w/c ratios (**Fig. 9**). This observation is consistent with the findings that creep characteristic times are virtually invariant over length scales [86].

Similar limitations of logarithmic functions in describing the creep behavior of CSH at the microscale have not only been reported for MCBs [34], but have also been observed recently in compressive creep tests of cementitious micropillars [87]. Based on the above observations, the power function is adopted in the following simulation, which will be detailed in section 5.4.

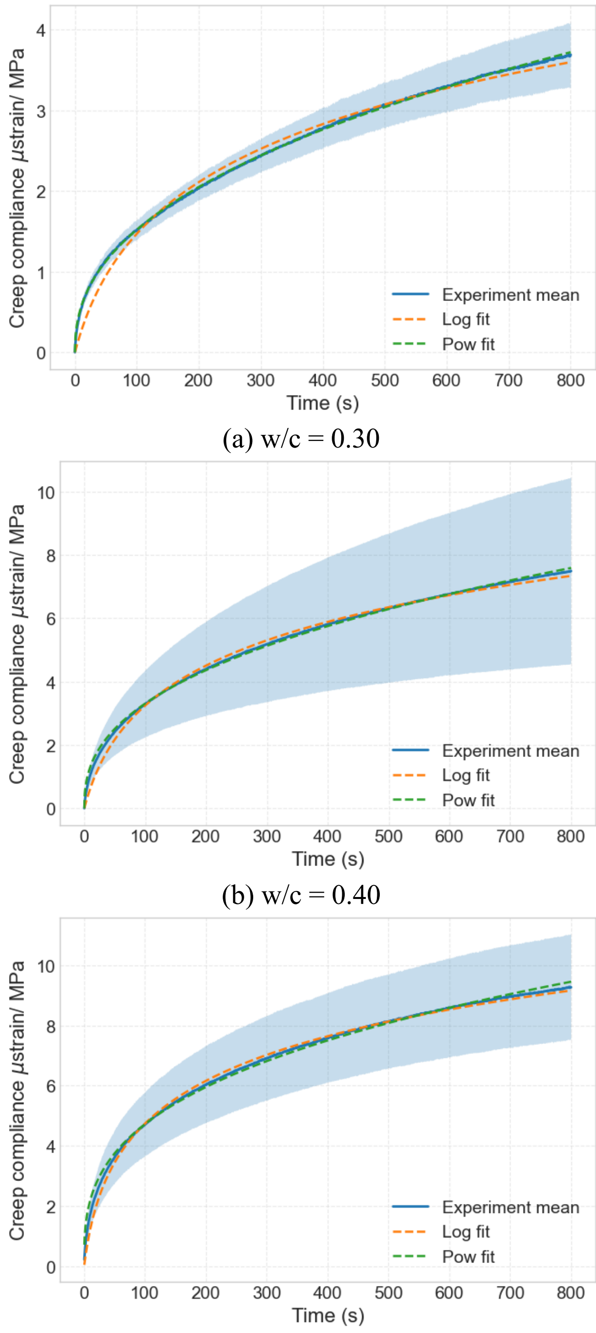

(a) w/c = 0.30

(b) w/c = 0.40

(c) w/c = 0.50

Fig. 8 Fitting the creep function with power and logarithmic functions for experimental results of MCB creep tests with w/c = 0.30 (a), 0.40 (b), and 0.50 (c).

Table. 2 Fitting results of the creep function

w/c	a/ GPa		b		RMSE		R^2	
	Pow	Log	Pow	Log	Pow	Log	Pow	Log
0.30	4761	842	0.430	0.024	0.017	0.088	1.000	0.989
0.40	1903	453	0.399	0.034	0.065	0.125	0.998	0.994
0.50	982	446	0.333	0.073	0.117	0.123	0.996	0.996

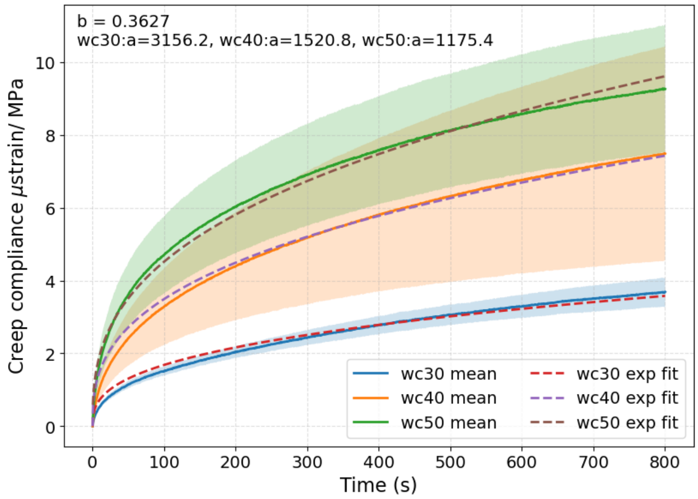

Fig. 9 Fitting the creep function with a one-parameter power function for experimental results of MCB creep tests

5.2 Microstructure resolution

This section presents the effects of microstructure resolution and mesh size of the simulated mechanical properties. It should be noted that the classical mesh-dependence issue in finite element analysis is addressed in the present framework through energy regularization (Eqs. 12b and 13c), and further details can be found in [40]. Here, however, the mesh size plays a different role. Varying the finite element mesh size leads to microstructural inputs with different spatial resolutions (see **Fig. 7**), which in turn affects the predicted mechanical response.

To investigate this effect, four different mesh sizes were considered, resulting in distinct microstructural phase assemblages. The results show that increasing the mesh size significantly alters the phase assemblage (**Fig. 10**). Coarse meshes tend to homogenize the microstructures and suppress phases with small volume fractions. Consequently, the volume fractions of pores (**Fig. 10a**) and UHC (**Fig. 10b**), which constitute relatively small portions of the composite, are progressively underestimated as the mesh size increases. In contrast, the dominating phases, such as HD-CSH for w/c =0.30 (**Fig. 10c**) and LD-CSH for w/c =0.50 (**Fig. 10d**), will be overestimated. As a result, microstructures generated with larger mesh sizes exhibit reduced porosity and higher degree of hydration, indicating enhanced micromechanical properties.

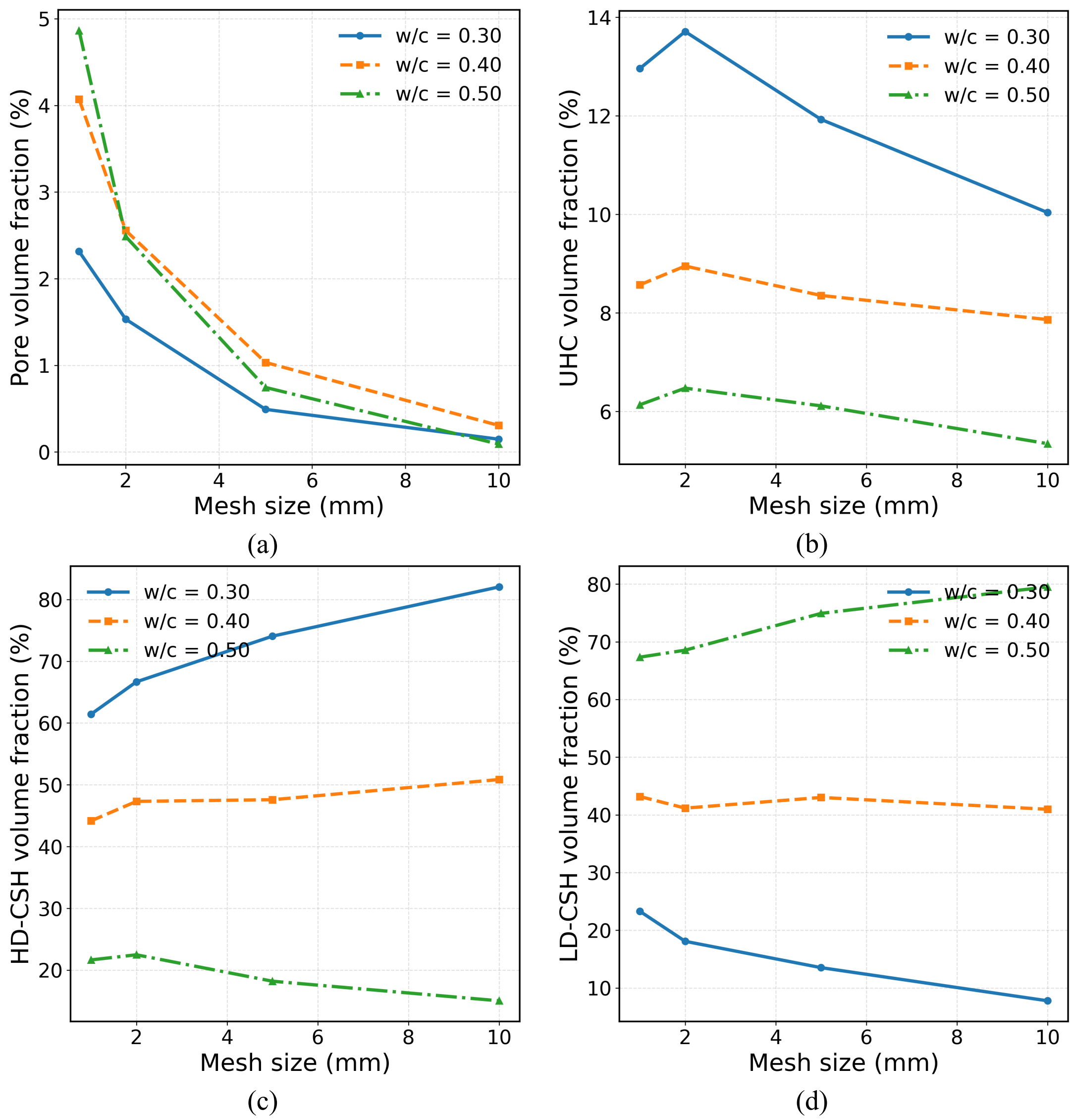

Fig. 10 Phase assemblage of microstructures with different resolutions: (a~b) correspond to the volume fraction of pores, LD-CSH, HD-CSH, and UHC.

For each mesh size, microstructures corresponding to three different w/c ratios were extracted at 6 different depths. Virtual flexural tests were then conducted using the proposed model by applying a prescribed displacement at the rate of 3 μm/s, leading to flexural failure of the MCBs. Note that due to the small specimen size, each MCB specimen samples a distinct local arrangement of different phases, which further leads to scattering in the results. For larger specimens approaching the cement-paste RVE, this scatter is expected to decrease. Based on these virtual tests, the influence of mesh size on the flexural strength and elastic modulus was evaluated, as shown in **Fig. 11**. Both the flexural strength and elastic modulus increase with increasing mesh size, which can be explained by the reduced porosity and increased hydration degree as illustrated by the **Fig. 10** and consistent with studies on the effect of pores on mechanical properties [88].

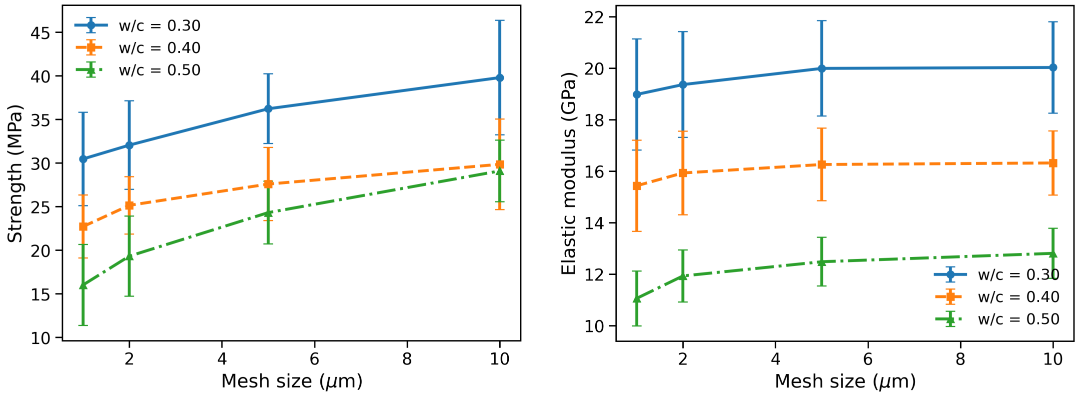

(a) Strength (b) Elastic modulus

Fig. 11 Influence of microstructure resolution on the strength and elastic modulus

Representative failure patterns obtained using different mesh sizes are shown in **Fig. 12**. In all cases, damage localizes near the upper clamping region, while the remainder of the beam remains largely undamaged, indicating a brittle failure mode. For the fine mesh, damage is more widespread and spatially dispersed, with multiple damaged zones activated within the microstructure (**Fig. 12(a), top**). This behavior is accompanied by a more heterogeneous distribution of the first principal stress with higher peak levels (**Fig. 12(a), bottom**). In contrast, the coarse mesh exhibits a highly localized damage pattern dominated by a single crack (**Fig. 12(b), top**), together with a smoother and more uniform principal stress field (**Fig. 12(b), bottom**). The reduced microstructural resolution suppresses local stress levels, leading to a higher apparent strength. For clarity of comparison, the stress contours of the fine mesh are plotted using the same color scale as the coarse mesh, although the actual maximum principal stress reaches approximately 60 MPa for the fine mesh, compared with about 45 MPa for the coarse mesh.

In general, the mesh size and microstructural resolution exert a significant influence on the predicted strength and elastic modulus. It should be noted that the monotonic rise of strength and modulus with mesh size indicates that the present voxel-based, discrete-phase CT–FEM does not converge under mesh refinement in the classical sense — a well-known limitation of CT-based FEM in which per-element single-property assignment loses sub-element heterogeneity [89]. Reported remedies include intravoxel micromechanics [89] or image-based deep learning [63]. Herein, the mesh size of 2 μm is tentatively retained as a practical engineering compromise, with the residual mesh-size dependence acknowledged as a structural limitation, to be addressed in future work via continuous material mapping. It is also acknowledged that the porosity and hydration degree obtained from the segmented microstructures were not independently validated against experimental measurements, e.g., mercury intrusion porosimetry (MIP) or quantitative X-ray diffraction with Rietveld refinement, in the present work.

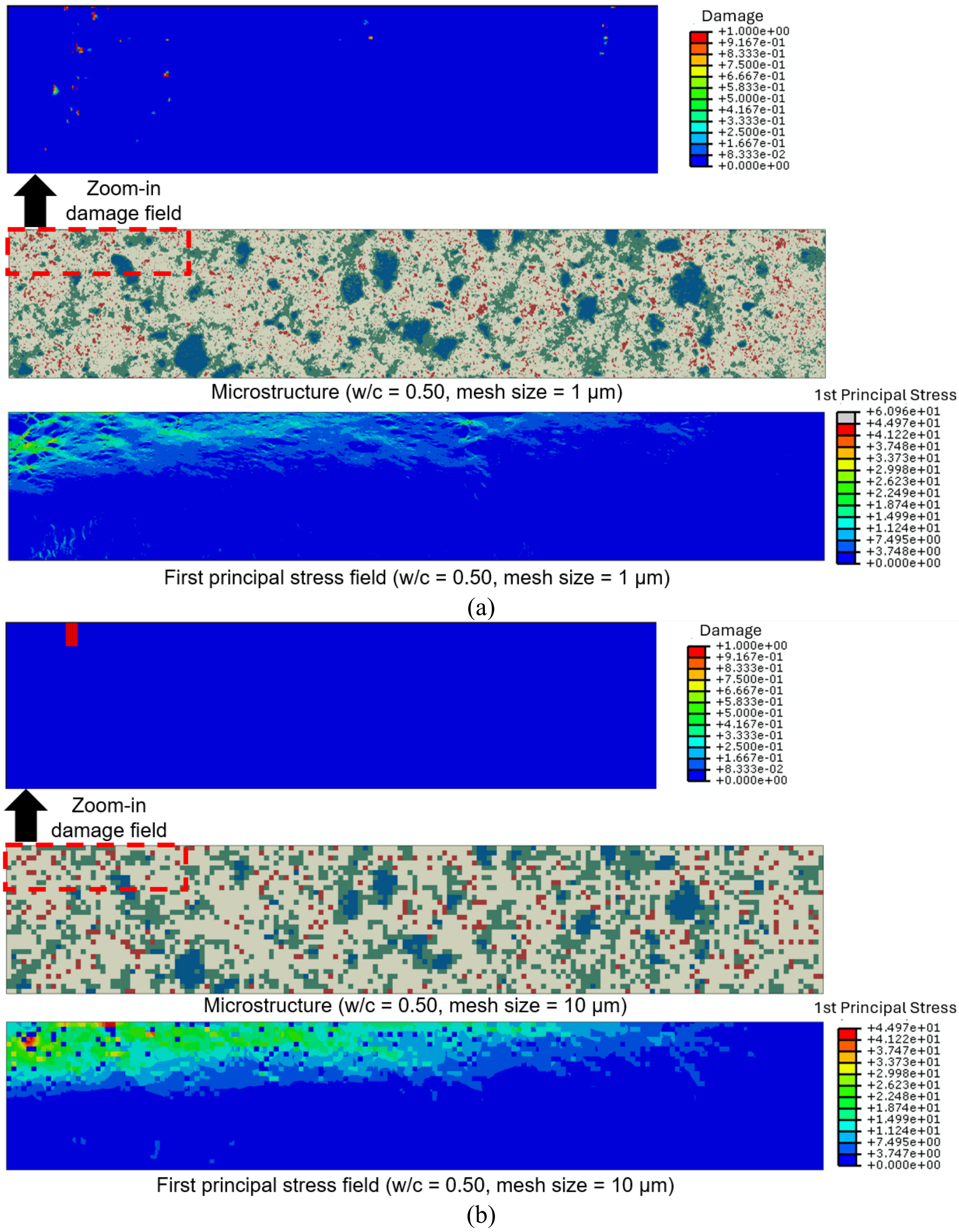

Fig. 12 Damage and first principal stress of microstructures of w/c = 0.50 with mesh sizes of 1 μm (a) and 10 μm (b)

5.3 Flexural strength and elastic modulus

This section compares the model predictions of flexural strength and elastic modulus with the results obtained from static bending tests on MCBs [40]. A vertical downward displacement was applied at the free end of the MCB at a constant rate of 50 nm/s, consistent with the experimental setup. Using the 2 μm mesh size selected in Section 5.2, microstructures corresponding to three different w/c ratios were extracted at eight different depths. The elastic modulus, tensile strength, and fracture energy listed in Table 1 were calibrated using the experimental results for w/c = 0.30, and the calibrated parameters were subsequently employed to predict the mechanical response of specimens with w/c = 0.40 and 0.50.

Overall, the predicted flexural strength and elastic modules show good agreement with the experimental data (Fig. 13). As the w/c ratio decreases, the model correctly captures the increasing trend in both elastic modulus and flexural strength. In addition, the simulated load–displacement curves (**Fig. 14**) reproduce the brittle mechanical response observed in the experiments, characterized by a sudden loss of load-carrying capacity associated with catastrophic failure of the MCBs [73]. Interestingly, although with a much lower strength, the results of w/c =0.50 show a similar ultimate failure displacement with the w/c =0.30. This is due to the much lower elastic modulus of the LD-CSH (main phase in w/c=0.50) than the HD-CSH (main phase in w/c=0.30), which directly determines the initiation of damage according to Eq. (8).

It is also worth noting that, the pronounced brittleness observed in simulations is strongly influenced by the tensile fracture energy G_{fIt}, which was set to 0.5 and 1.0 J/m² for LD- and HD-C–S–H, respectively. These values are consistent with typical ranges reported in molecular dynamics simulations of crack nucleation and propagation in CSH at the atomic scale [74–76]. Note that the compressive damage parameters were not independently calibrated in this study. For future applications involving compression-dominated loading scenarios, independent calibration of these parameters would be necessary.

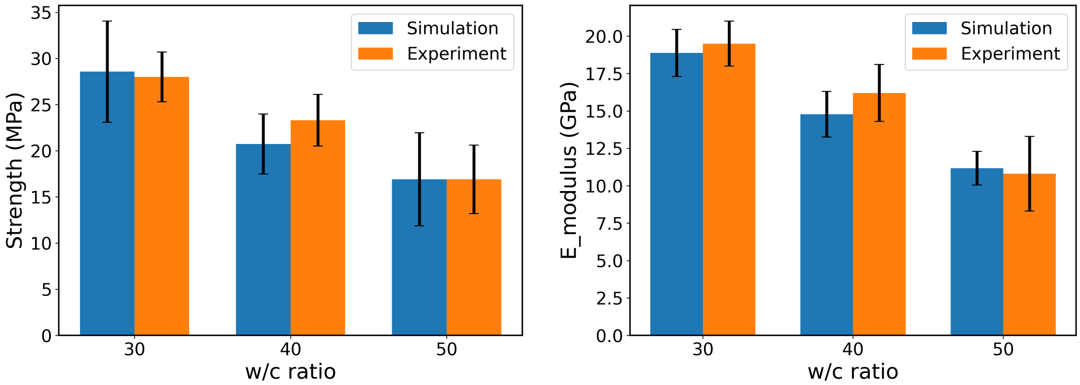

(a) (b)

Fig. 13 Comparison of the experimental and numerical results on flexural strength (a) and elastic modulus (b)

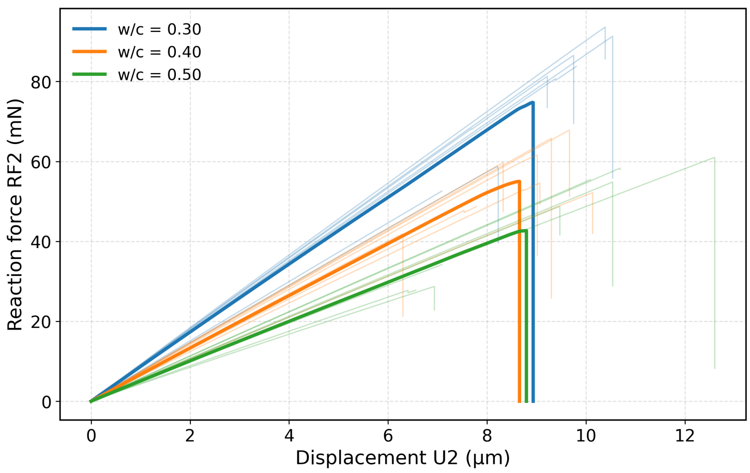

Fig. 14 Load-displacement curves in virtual static bending tests

5.4 Linear creep at low stress level

This section presents the predicted linear creep compliance at a low stress level and its comparison with the experimental results reported in [34]. Following the experimental configuration (**Fig. 2c**, left), the load is applied at the free end of the MCBs. The load is first increased to 30% of the maximum force (**Fig. 14**) at a constant rate of 2 mN/s, and then held constant for 800 s, during which creep deformation develops. At this stress level, the damage variable remains effectively zero throughout the creep phase. The creep compliance is subsequently calculated based on classical cantilever beam theory. Note that this section only deals with linear creep at low stress level. Nonlinear creep at high stress level can be found in section 5.5.

Prior to the simulation, the parameters of the creep function for each individual phase—expressed as a power-law function in Eq. (29a)—must be calibrated. This creep function is governed by two parameters: the creep modulus and the exponent. Although extensive micro-indentation studies have been conducted to characterize the viscoelastic properties of CSH and cement paste [12,22,83], a clear discrepancy between indentation tests and MCB or micropillar creep experiments has been reported, indicating that micro-indentation data cannot be directly applied to simulate MCB creep behavior [35,87]. In this study, the exponent is assumed to be identical for all phases, and the creep moduli of LD- and HD-CSH are calibrated using the creep compliance results of the specimen with w/c = 0.30. The UHC phase is treated as an almost elastic inclusion, with a creep modulus significantly higher than those of the CSH phases. Two values of the creep exponent are considered based on two different assumptions:

1) The creep of the CSH phases follows the same temporal evolution as the cement paste composite, leading to an exponent of 0.36, adopted from the fitting results in **Fig. 9**;
2) The creep of the cement paste composites evolves faster than that of the CSH phases due to the weakening effects of the pores. With such assumption, a smaller exponent of 0.20 is tentatively assumed for the CSH phases.

For each exponent, the corresponding creep modules are calibrated independently. The Kelvin chain representation corresponding to the adopted exponent is derived from Eq. (28) using an order of three (i.e., $k = 3$), and the resulting spectrum ($E_j, \mathrm{j} = 1\sim 9$) is summarized in **Table 3**. This configuration has been validated in previous studies [90–92] and yields stable, converged spectra for the viscoelastic behaviors. Note that each chain unit is described by a coefficient A_j:

$$E_j = A_j E_{cr} \tag{30}$$

Table. 3 Continuous Kelvin Chain Spectrum

	j	1	2	3	4	5	6	7	8	9
A_j	$b = 0.36$	0.020	0.048	0.112	0.262	0.611	1.422	3.308	7.696	17.906
	$b = 0.20$	0.065	0.103	0.164	0.260	0.413	0.654	1.030	1.640	2.606

Using the two Kelvin chain representations as input, the creep modulus is calibrated based on the creep compliance curves of the specimen with w/c = 0.30. The calibrated parameters are then employed to predict the creep behavior of specimens with w/c = 0.40 and 0.50. As shown in **Fig. 15**, both models yield good agreement with the experimental creep compliance curves. Notably, the agreement achieved by the exponent (b=0.36) aligns with the findings of Binder et al. [86], who used continuum micromechanics homogenization to show that volume-averaged phase stresses remain virtually constant during short-term creep of cement paste, implying that the creep exponent is scale-invariant. Nevertheless, the lower exponent consistently yields lower RMSE and higher R^2 values, indicating that local stress concentrations around pores may accelerate the composite creep kinetics. Ultimately, direct microscale creep tests on pure CSH phases compared with their corresponding composites would be needed to verify this conclusion.

An additional noteworthy observation concerns the calibrated creep modulus obtained for the two different creep exponents (**Table 4**). A clear discrepancy is evident in the absolute values of the creep modulus associated with different exponents, which strongly cautions against the practice of using the creep modulus alone as the sole indicator of viscoelastic properties. Overall, the creep modulus of HD-CSH is approximately 4–5 times higher than that of LD-CSH, a ratio that is significantly larger than the values of 1–2 commonly reported in micro-indentation studies [12,82].

However, this ratio becomes less surprising when the creep behavior of cement paste composites with different w/c ratios is further examined. As shown in **Fig. 9**, the creep modulus of the cement pastes composite decreases from approximately 3150 GPa at w/c = 0.30 to about 1170 GPa at w/c = 0.50. Notably, these values are of a similar magnitude and reasonably consistent with the calibrated creep modules of HD-CSH (≈3000 GPa) and LD-CSH (≈700 GPa), when the same power-law exponent of 0.36 is employed. The remaining differences may be attributed to the contribution of other phases and calibration uncertainties. It should be noted that the microstructures of w/c = 0.30 and 0.50 are dominated by HD-CSH and LD-CSH (**Fig. 10**), and their creep tests primarily reflect the properties of these two phases respectively. From this perspective, the disparity between the calibrated creep modules of LD- and HD-CSH is consistent with the experimental trends observed at different w/c ratios.

From a mechanistic standpoint, the discrepancy with micro-indentation data is primarily attributed to the two-phase (LD-/HD-CSH) segmentation of the hydration products adopted in this work, which follows the Jennings model [57] and does not separately account for CH, which was found to enhance the creep moduli of CSH more strongly than its elastic moduli [93]. At low w/c, nanoscale CH and CSH tend to coexist as an intimate nanocomposite that has been identified as ultra-high-density (UHD) CSH [94]. At higher w/c, the larger precipitation space may instead favor separate, larger Portlandite crystals, which should be treated as a separate CH phase. The present segmentation absorbs CH into HD-CSH in both cases, which explains the elevated HD/LD creep-modulus ratio obtained here. More refined segmentation strategies, such as AI- or ML-based microstructure segmentation from higher-resolution images [95] (e.g., BSE-SEM coupled with EDS mapping), are recommended for future work to enable more accurate intrinsic creep properties to be determined for each phase.

Table. 4 Creep modulus (E_{cr}) for the CSH phases calibrated from the experiments (GPa)

	LD-CSH	HD-CSH
$b = 0.36$	700	3000
$b = 0.20$	170	820

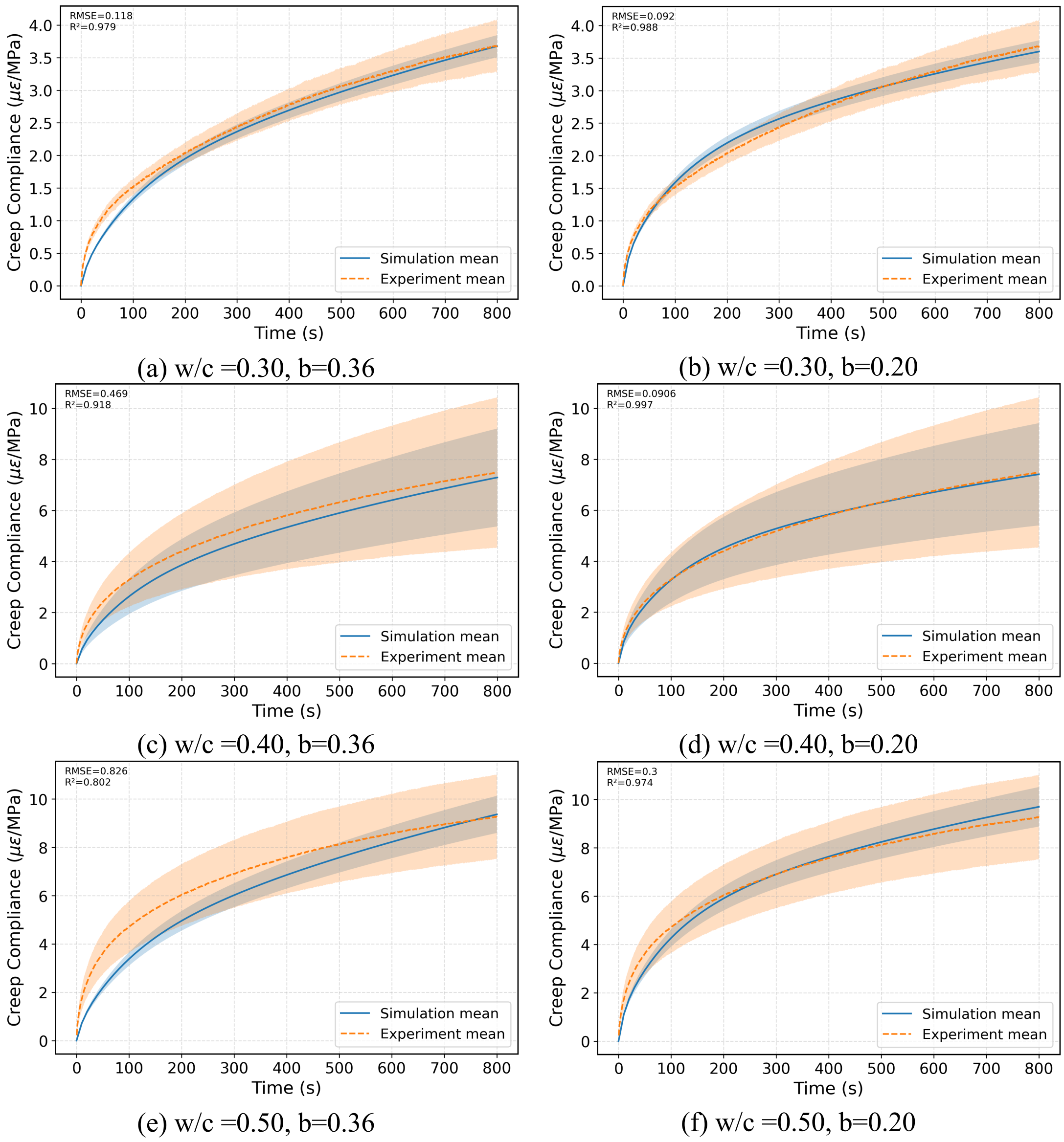

(a) w/c =0.30, b=0.36 (b) w/c =0.30, b=0.20

(c) w/c =0.40, b=0.36 (d) w/c =0.40, b=0.20

(e) w/c =0.50, b=0.36 (f) w/c =0.50, b=0.20

Fig. 15 Comparison of the experimental and predicted creep compliance curves for different w/c ratios: (a, c, e) and (b, d, f) are the results predicted using power function with the exponent b adopted as 0.36 and 0.20, respectively.

5.5 Creep recovery and nonlinear creep

This section presents predicted creep recovery at different stress levels and demonstrates the nonlinear creep that could happen at high stress level. The predicted creep recovery is compared with the experimental results [35]. Note that here only w/c =0.30 and 0.40 will be compared and discussed since only these two w/c ratios were investigated in the experiments. Following the experimental settings (**Fig. 2c**, middle), the load is applied at the free end of the MCBs. The loading scheme contains four stages: 1) In 5s, the load is firstly increased to three different levels: 45%, 70%, and 90% of the maximum force; 2) The load is kept constant for 180s to induce creep deformation; 3) In 5s, the load is decreased to 1% of the maximum force; 4) The small load is then sustained for 600s to enable creep recovery. Note that the parameters related to the strength and linear creep have been calibrated in section 5.3 and 5.4 and will be directly adopted herein for the prediction here. The other parameters are calibrated again using the w/c =0.30 results and validated by the results at w/c =0.40.

A typical deformation history resulting from the loading scheme described above is shown in **Fig. 16**, using a virtual specimen with w/c = 0.30 as an example. The creep deformation accumulated during 5–185s and the subsequent creep recovery during 190–790s are used to compute the creep recovery ratio, which is directly compared with the experimental results as shown in **Fig. 17**. Overall, the predicted recovery ratios show good agreement with the experiments. Both specimens with w/c = 0.30 and 0.40 exhibit high recovery ratios (~0.90) at a stress level below 70%, indicating a predominantly linear creep behavior at these two stress levels. Note that the predicted recovery ratios in **Fig. 17** are averaged over microstructures extracted at eight different depths. However, it was found that the creep recovery ratio remains almost the same for different depths, which can be attributed to the linear creep behavior at low stress level. In this study, different phases are assigned to a different creep modulus, but with the same Kelvin chain indicating similar temporal evolution trend of creep (**Table. 3**). As a result, the creep modulus acts as a scaling factor on the deformation history. When the recovery ratio is computed as the ratio between creep recovery and creep deformation, the phase-dependent creep moduli is mathematically canceled out. Consequently, the recovery ratio is governed solely by the temporal creep evolution and remains insensitive to microstructural variations, leading to similar values for all depths.

At the high stress level (~90%), a decrease in the creep recovery ratio is observed, consistent with the experimental results (**Fig. 17**). Here, the damage leads to nonlinear creep and increases the irreversible viscous deformation (as described by Eq. (3.3)), which finally results in decrease of the recovery ratio. Unlike in the linear regime, the cancellation of phase-dependent creep moduli in the recovery ratio no longer holds at this stress level, as damage develops non-uniformly across the microstructure and the irreversible viscous strain does not recover upon unloading. As an example, the creep compliance of the virtual specimen with w/c =0.40 is shown in **Fig. 18**, which demonstrates an increased creep compliance curve at high stress level, indicating nonlinear creep behavior.

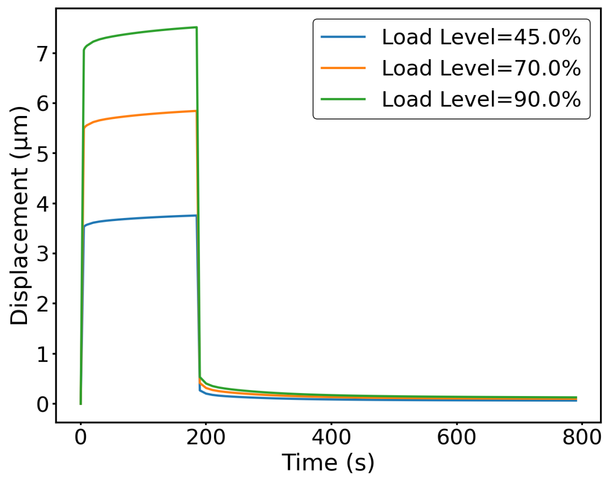

Fig. 16 The displacement history in the creep and creep recovery test for a virtual specimen with w/c =0.30 at different loading levels.

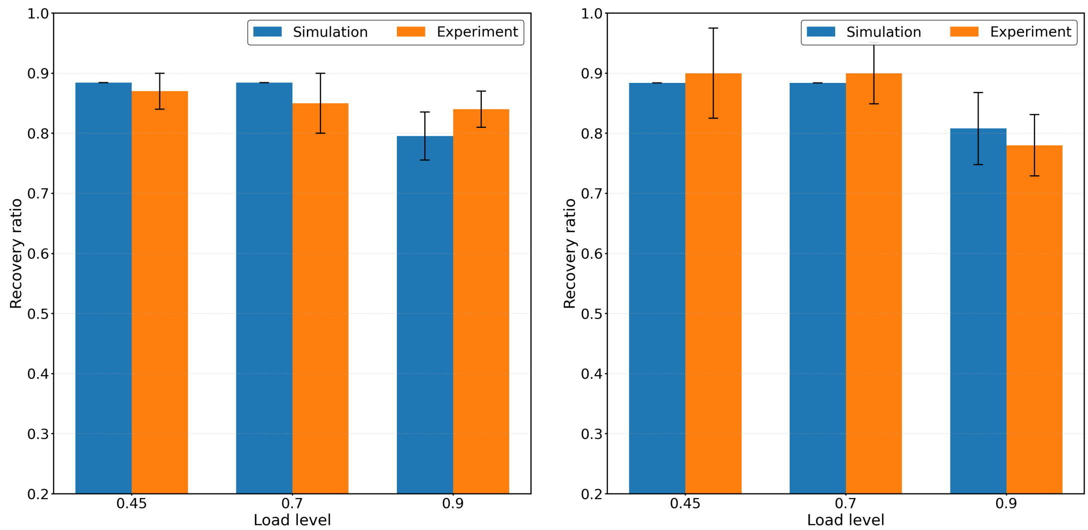

(a) w/c =0.30 (b) w/c = 0.40

Fig. 17 Comparison of the predicted and experimental creep recovery ratio

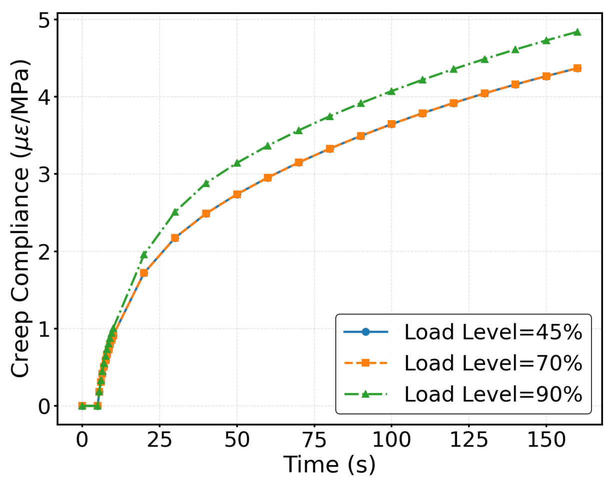

Fig. 18 Creep compliance at different loading levels for a virtual specimen with w/c =0.40 at different loading levels.

5.6 Strain rate effects

This section investigates the influence of loading strain rate on the static micromechanical properties of cementitious composites. Following the experimental setup illustrated in **Fig. 2c (right)**, a downward displacement is applied at the free end of the MCB under different loading strain rates. For specimens with w/c = 0.30 and w/c = 0.40, the applied strain rates range from 1.3 to 4341.7 με/s and from 0.7 to 5043.6 με/s, respectively. Based on these simulations, the elastic modulus and flexural strength of the virtual specimens are predicted and compared with the corresponding experimental results reported in [36]. All material parameters used herein were calibrated in the previous sections.

As shown in **Fig. 19**, the modelling results exhibit reasonable agreement with experimental observations. Both the elastic modulus and flexural strength increase with increasing loading strain rate, which is consistently captured by the coupled creep–damage framework. This trend is physically reasonable: slower loading rates correspond to longer loading durations, allowing creep deformation to develop and induce additional damage, thereby reducing both stiffness and strength [96].Such rate-dependent behavior is intrinsically represented in Eq. (17–19), which describe a two-way coupling mechanism. On the one hand, creep strain contributes to the equivalent strain and accelerates damage evolution; on the other hand, damage reduces the effective elastic modulus, increasing the stress carried by the Kelvin chain components and thus enhancing creep development. **Fig. 20** illustrates the creep strain distribution of a representative virtual specimen with w/c = 0.30 prior to damage initiation. The maximum creep strain is concentrated near the upper clamping region of the MCB, where tensile stresses dominate and damage is prone to initiate. Notably, the peak creep strain at the slowest loading rate ($\sim 10^{-4}$) is approximately one order of magnitude higher than that at the fastest loading rate ($\sim 10^{-5}$), leading to accelerated equivalent strain accumulation, enhanced damage evolution, and ultimately reduced elastic modulus and strength.

Despite the overall consistency, an abrupt increase in the experimentally measured properties is observed at the highest loading rate, which is not fully reproduced by the model. At this rate, the total loading duration is shorter than 1 s, suggesting the involvement of inertial effects and dynamic micromechanical responses. Since the present model is formulated within a quasi-static framework, such high-rate dynamic effects are beyond its current scope. Extending the present quasi-static formulation to a dynamic framework by incorporating inertial effects and rate-dependent constitutive laws can capture such high-rate responses.

The damage patterns of the virtual specimen with w/c = 0.30 under two representative loading rates are presented in **Fig. 21**. Compared with the slow loading case, the fast-loading rate leads to more pronounced damage features, as evidenced by a broader damaged region (**Fig. 21**, top) and stronger stress concentration (**Fig. 21**, bottom). Overall, the damage distribution under fast loading can be regarded as a more progressed version of that observed under slow loading. This trend is consistent with the experimental observations reported in [36]. In particular, quantitative image analysis in [36] showed that the volume fraction of UHC within the fracture profile increased from approximately 6.3% at the slowest loading rate to 9.6% at the fastest loading rate for specimens with w/c = 0.30. Since UHC and its surrounding HD-CSH are among the stronger phases in the composite, their increased involvement indicates a more severe damage process. The agreement between the experimental trend and the modelling results supports that the observed rate-dependent damage patterns are governed by the coupled creep–damage effects.

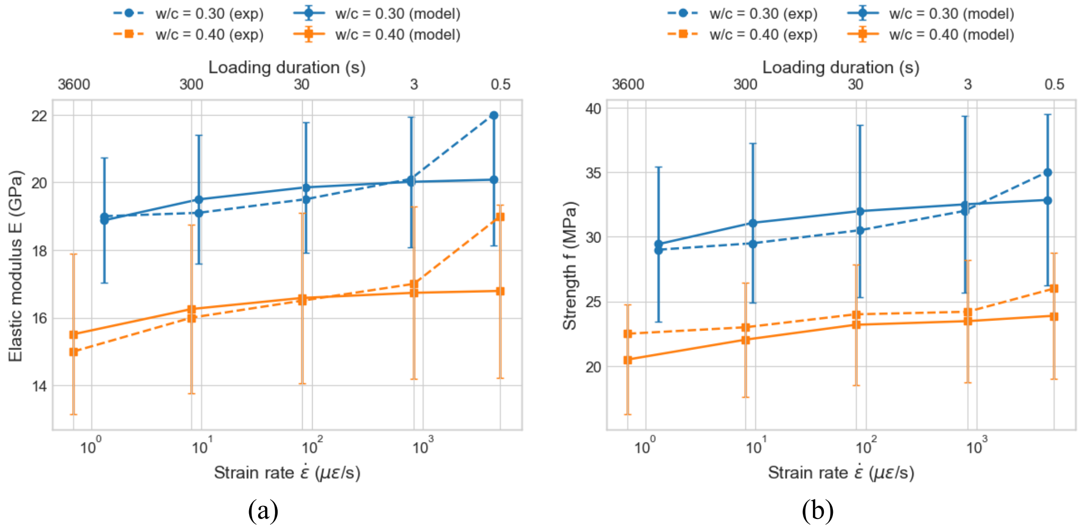

Fig. 19 Effects of the strain rate on the elastic modulus and flexural strength

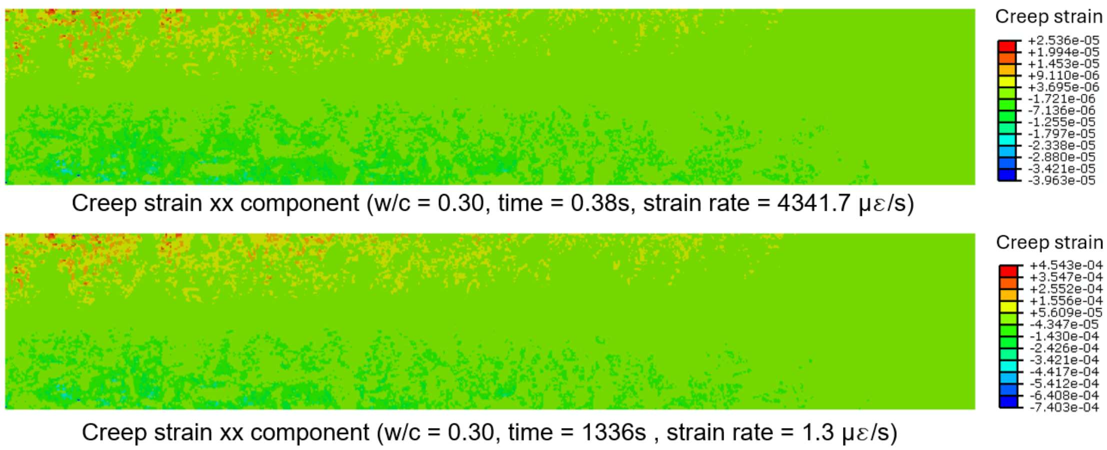

Fig. 20 Creep strain components of the virtual specimen with w/c =0.30 under different loading rates at the onset before damage

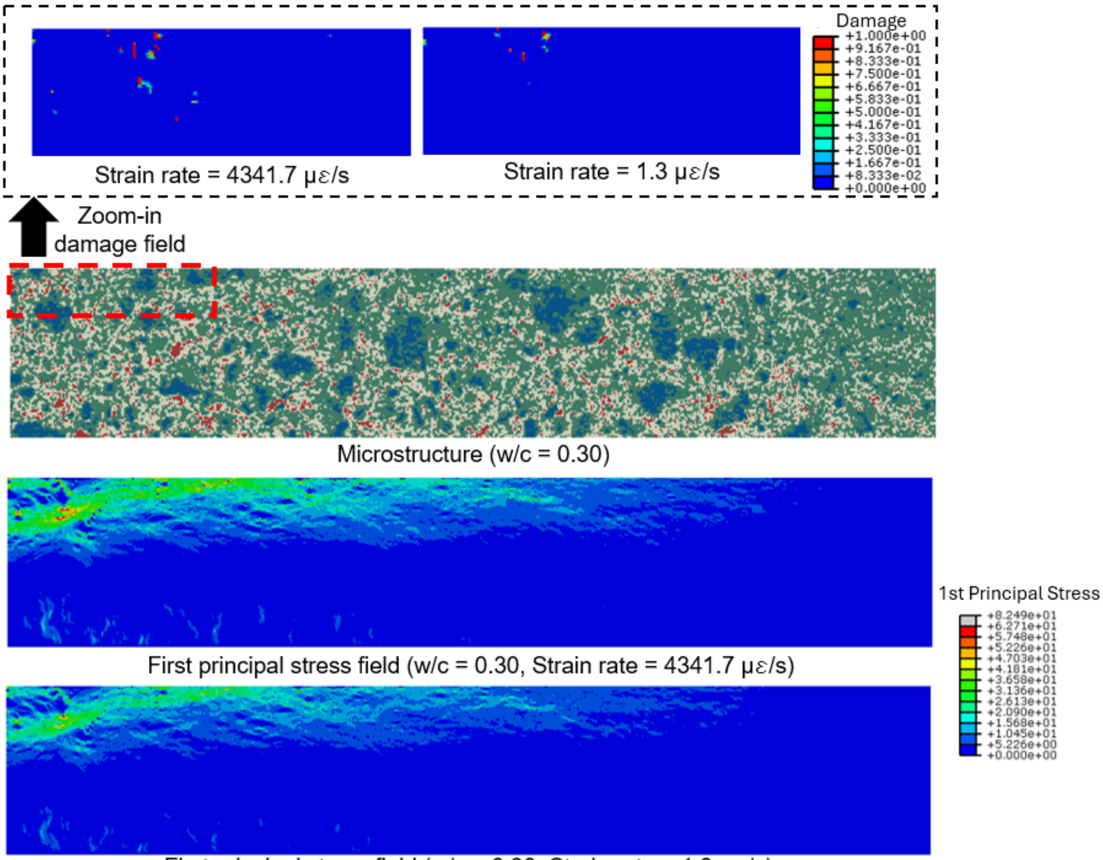

Fig. 21 Comparison of typical damage patterns of a virtual specimen with w/c =0.30 under different loading rates

Conclusions

This study proposed an experimentally informed coupled creep–damage modelling framework to investigate the time-dependent micromechanical behavior of hardened cement paste. By combining realistic microstructural inputs with a viscoelastic formulation based on an exponential algorithm and a continuum damage model, the framework enables a consistent description of creep, creep recovery, and strain-rate-dependent failure at the microscale. The main conclusions can be summarized as follows.

1) Microstructural resolution has a strong influence on the predicted mechanical response. Coarse resolutions underestimate pores and unhydrated cement while overestimating CSH content and the degree of hydration, which directly leads to overestimated elastic modulus and flexural strength. In addition, the associated homogenized stress fields suppress local stress concentrations and delay damage initiation, further contributing to the overestimation of strength and stiffness. These results underscore the importance of resolving realistic microstructures when modelling microscale mechanical behavior.
2) The model predicts the flexural strength and elastic modulus for different w/c ratios and reproduces the pronounced brittle response observed experimentally. This brittleness is primarily governed by the tensile fracture energy, and the adopted fracture energy values for LD- and HD-CSH are consistent with reported ranges from molecular dynamics studies, supporting the physical consistency of the model.
3) The model predicts linear creep at low stress levels, with the power-law creep function showing clear advantages over the logarithmic formulation. Improved agreement is obtained when a lower creep exponent is adopted, indicating that the intrinsic creep of CSH phases evolves more slowly than the apparent creep of the cement paste composite. The pronounced ratio of creep modulus between LD- and HD-CSH, although differing from microindentation results, is consistent with that observed in cement pastes with w/c = 0.50 and 0.30, which are dominated by LD- and HD-CSH, respectively. This difference is primarily induced by the effect of CH, which strongly increases the creep modulus of CSH

and is implicitly included in the HD-CSH phase in this study. This finding highlights the importance of accurately quantifying effects of CH on creep of CSH when simulating microscale creep behavior.

4) The model predicts creep recovery at different stress levels, showing good agreement with experimental results. At stress levels below approximately 70% of the flexural strength, both simulations and experiments exhibit high recovery ratios (≈0.90), indicating a predominantly linear creep behavior. In this linear regime, similar recovery ratios are obtained for microstructures extracted at different depths, as different phases are assigned to different creep moduli but share the same Kelvin chain and temporal evolution of creep, so that the phase-dependent creep moduli are mathematically canceled out when computing the recovery ratio. At higher stress levels, reduction in recovery ratio and increase of creep compliance are observed due to damage.
5) The model captures the strain-rate-dependent mechanical response of cement paste at the microscale, showing good agreement with experiments in terms of both elastic modulus and flexural strength. In addition, the simulated damage patterns closely resemble the experimental observations: slow loading promotes creep-induced damage initiation in weaker phases, leading to localized failure, whereas fast loading results in more extensive and severe damage propagating into stronger phases. This consistency indicates that the proposed framework captures the underlying coupling between creep and damage at the microscale. At the highest loading rates, deviations from experimental results are observed, suggesting the involvement of dynamic micromechanical effects, which are beyond the scope of the present quasi-static formulation.

Overall, the proposed coupled creep-damage framework provides a physically consistent and computationally efficient approach for predicting the time-dependent micromechanical behavior of hardened cement paste. Future work may focus on incorporating environmental effects such as moisture and temperature to capture time-dependent behavior under more realistic service conditions. In addition, the present microscale model may serve as a constitutive building block within a multiscale modelling framework, in which the effects of aggregates, reinforcement, and interfacial transition zones are accounted for, enabling simulations of long-term mechanical performance of concrete structures.

Appendix A. Sensitivity of the LD/HD threshold (S2)

As discussed in Section 4.1, the LD/HD threshold S2 depends on the discrete-cluster assumption. To quantify how the FE predictions respond to perturbations of S2 with S1 and S3 fixed, the w/c = 0.30 specimen was re-segmented with three values:

- *S2_base*: used in the main paper; prescribed by the Tennis–Jennings model.
- *S2_low*: midpoint of the LD greyscale range, yielding 77.8 % HD-CSH — over-emphasises HD beyond the Tennis–Jennings model.
- *S2_high*: midpoint of the HD greyscale range, yielding 65.1 % LD-CSH — inconsistent with the HD-dominance expected for low w/c paste.

Both perturbations deliberately depart from the physically motivated value of S2_base. **Fig. A1** shows the segmented microstructure at depth slice 60 for each variant; Pore and UHC regions are identical across the three variants since S1 and S3 are unchanged.

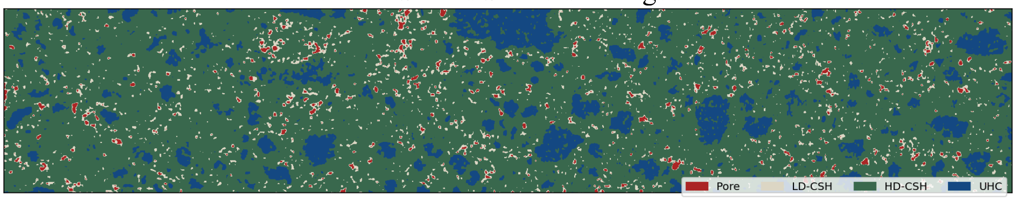

(a) *S2_low*

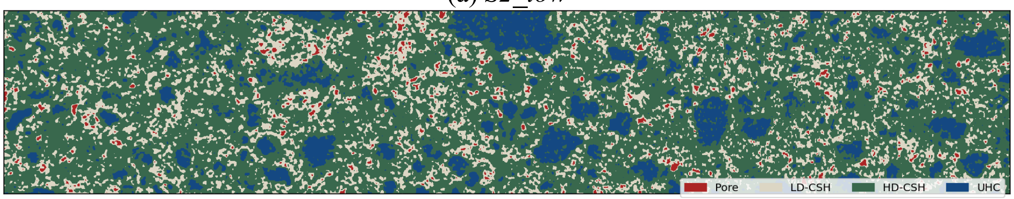

(b) *S2_base*

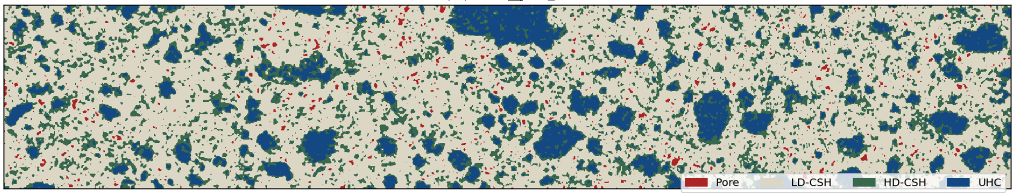

(c) *S2_high*

Fig. A1 Segmented microstructures with different LD/HD threshold (S2) with w/c =0.30

The static cantilever bending simulation described in Section 5.3 was run on four depth slices per variant. Strength and modulus normalized to S2_base are shown in **Fig. A2**.

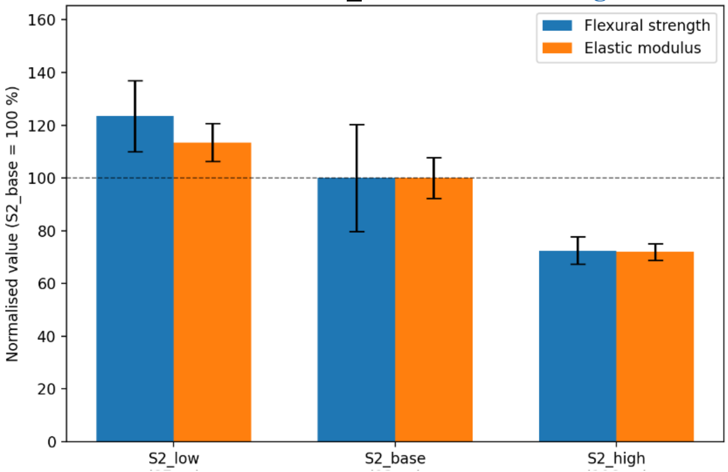

Fig. A2 Simulated strength and elastic modules of microstructures with w/c =0.30 segmented by different LD/HD threshold (S2)

The perturbations shift the predictions by +24 %/−27 % in strength and +14 %/−28 % in modulus, with the model responding in a physically reasonable direction (i.e., more HD results in stronger and stiffer mechanical properties). These results bound the residual uncertainty introduced by the binary LD/HD simplification within ±28 % under deliberately unphysical perturbations of the LD/HD threshold.

Acknowledgements

Minfei Liang and Sonia Contera would like to acknowledge the funding support provided by the European Union within the Project 'ZEBAI - Innovative methodologies for the design of Zero-Emission and cost-effective Buildings enhanced by Artificial Intelligence' HORIZON-CL5-2023-D4-01-01 [grant agreement No: 101138678, DOI 10.3030/101138678]. Yong Fang acknowledges the support of the National Science Fund for Distinguished Young Scholars (Grant No.52425807). Yidong Gan would like to acknowledge the funding supported by the National Natural Science Foundation of China (Grant No. 52408261). Wenqi Guo would like to acknowledge the funding supported by the National Natural Science Foundation of China (Grant No. 52508458). Chuan He acknowledges the support of the National Natural Science Foundation of China (NSFC) under Grant No. U25A6017 ("Fundamental Problems in Intelligent Construction of Long and Large Tunnels in Extreme Environments of Western Mountainous Areas"). Branko Šavija acknowledges the financial support of the European Research Council (ERC) within the framework of the ERC Starting Grant Project "Auxetic Cementitious Composites by 3D printing (ACC-3D)", Grant Agreement Number 101041342.

Reference

[1] A.M. Neville, Properties of concrete-5th edition, 2011.

[2] M. Liang, J. Xie, S. He, Y. Chen, E. Schlangen, B. Šavija, Autogenous deformation-induced stress evolution in cementitious materials considering viscoelastic properties: A review of experiments and models, Dev. Built Environ. 17 (2024) 100356. https://doi.org/10.1016/j.dibe.2024.100356.

[3] M. Azenha, F. Kanavaris, D. Schlicke, A. Jędrzejewska, F. Benboudjema, T. Honorio, V. Šmilauer, C. Serra, J. Forth, K. Riding, B. Khadka, C. Sousa, M. Briffaut, L. Lacarrière, E. Koenders, T. Kanstad, A. Klausen, J.M. Torrenti, E.M.R. Fairbairn, Recommendations of RILEM TC 287-CCS: thermo-chemo-mechanical modelling of massive concrete structures towards cracking risk assessment, Mater. Struct. Constr. 54 (2021) 135. https://doi.org/10.1617/s11527-021-01732-8.

[4] S. Jiang, Y. Wang, Z. Cheng, B. Chen, Adaptive forecasting of stochastic crack growth using empirical mode decomposition: Gaussian process regression for structural health monitoring, Struct. Infrastruct. Eng. (2026) 1–14. https://doi.org/10.1080/15732479.2026.2617965.

[5] Z. P. Bazant, M. H. Hubler, Q. Yu, Pervasiveness of Excessive Segmental Bridge Deflections: Wake-Up Call for Creep, ACI Struct. J. 108 (2011). https://doi.org/10.14359/51683375.

[6] A. Hilaire, F. Benboudjema, A. Darquennes, Y. Berthaud, G. Nahas, Analysis of concrete creep in compression, tension and bending: Numerical modeling, in: Mech. Phys. Creep Shrinkage Durab. Conrete Tribute Zdenek P Bazant - Proc. 9th Int Conf Creep Shrinkage Durab. Mech. CONCREEP 2013, American Society of Civil Engineers (ASCE), 2013: pp. 348–355. https://doi.org/10.1061/9780784413111.041.

[7] S. Asamoto, K. Kato, T. Maki, Effect of creep induction at an early age on subsequent prestress loss and structural response of prestressed concrete beam, Constr. Build. Mater. 70 (2014) 158–164. https://doi.org/10.1016/j.conbuildmat.2014.07.028.

[8] O. Bernard, F.-J. Ulm, E. Lemarchand, A multiscale micromechanics-hydration model for the early-age elastic properties of cement-based materials, Cem. Concr. Res. 33 (2003) 1293–1309. https://doi.org/10.1016/S0008-8846(03)00039-5.

[9] W.R.L. da Silva, J. Němeček, P. Štemberk, Application of multiscale elastic homogenization based on nanoindentation for high performance concrete, Adv. Eng. Softw. 62–63 (2013) 109–118. https://doi.org/10.1016/j.advengsoft.2013.04.007.

[10] P. Havlásek, M. Jirásek, Multiscale modeling of drying shrinkage and creep of concrete, Cem. Concr. Res. 85 (2016) 55–74. https://doi.org/10.1016/j.cemconres.2016.04.001.

[11] F. Lavergne, J.F. Barthélémy, Confronting a refined multiscale estimate for the aging basic creep of concrete with a comprehensive experimental database, Cem. Concr. Res. 136 (2020). https://doi.org/10.1016/j.cemconres.2020.106163.

[12] Z. Hu, A. Hilaire, J. Ston, M. Wyrzykowski, P. Lura, K. Scrivener, Intrinsic viscoelasticity of C-S-H assessed from basic creep of cement pastes, Cem. Concr. Res. 121 (2019) 11–20. https://doi.org/10.1016/j.cemconres.2019.04.003.

[13] Z. Hu, A. Hilaire, M. Wyrzykowski, P. Lura, K. Scrivener, Visco-elastic behavior of blended cement pastes at early ages, Cem. Concr. Compos. 107 (2020) 103497. https://doi.org/10.1016/J.CEMCONCOMP.2019.103497.

[14] Z.P. Bažant, G. Cusatis, L. Cedolin, Temperature Effect on Concrete Creep Modeled by Microprestress-Solidification Theory, J. Eng. Mech. 130 (2004) 691–

699. https://doi.org/10.1061/(ASCE)0733-9399(2004)130:6(691).

[15] P. Rossi, J.-L. Tailhan, F. Le Maou, L. Gaillet, E. Martin, Basic creep behavior of concretes investigation of the physical mechanisms by using acoustic emission, Cem. Concr. Res. 42 (2012) 61–73. https://doi.org/10.1016/j.cemconres.2011.07.011.

[16] M. Wyrzykowski, K. Scrivener, P. Lura, Basic creep of cement paste at early age - the role of cement hydration, Cem. Concr. Res. 116 (2019) 191–201. https://doi.org/10.1016/j.cemconres.2018.11.013.

[17] Y. Li, Y. Liu, Y. Li, Y. Li, R. Wang, Evaluation of concrete creep properties based on indentation test and multiscale homogenization method, Cem. Concr. Compos. 123 (2021) 104135. https://doi.org/10.1016/J.CEMCONCOMP.2021.104135.

[18] Y. Li, Y. Liu, Z. Wang, H. Li, J. Mu, Effect of phases on the creep properties of cement paste based on indentation test and homogenization scheme, Constr. Build. Mater. 317 (2022) 125957. https://doi.org/10.1016/j.conbuildmat.2021.125957.

[19] S. Liang, Y. Wei, Imperfect Interface Effect on Creep Property of Hardened-Cement Pastes: Investigations from Nano to Micro Scales, J. Mater. Civ. Eng. 32 (2020) 04020173. https://doi.org/10.1061/(ASCE)MT.1943-5533.0003238.

[20] J. Baronet, L. Sorelli, J.P. Charron, M. Vandamme, J. Sanahuja, A two-scale method to rapidly characterize the logarithmic basic creep of concrete by coupling microindentation and uniaxial compression creep test, Cem. Concr. Compos. 125 (2022). https://doi.org/10.1016/j.cemconcomp.2021.104274.

[21] S. Liang, Y. Wei, Effects of water-to-cement ratio and curing age on microscopic creep and creep recovery of hardened cement pastes by microindentation, Cem. Concr. Compos. 113 (2020) 103619. https://doi.org/10.1016/j.cemconcomp.2020.103619.

[22] S. Mallick, M.B. Anoop, K. Balaji Rao, Early age creep of cement paste - Governing mechanisms and role of water-A microindentation study, Cem. Concr. Res. 116 (2019) 284–298. https://doi.org/10.1016/J.CEMCONRES.2018.12.004.

[23] M. Königsberger, M. Irfan-ul-Hassan, B. Pichler, C. Hellmich, Downscaling Based Identification of Nonaging Power-Law Creep of Cement Hydrates, J. Eng. Mech. 142 (2016) 04016106. https://doi.org/10.1061/(ASCE)EM.1943-7889.0001169.

[24] M. Königsberger, T. Honório, J. Sanahuja, B. Delsaute, B.L.A. Pichler, Homogenization of nonaging basic creep of cementitious materials: A multiscale modeling benchmark, Constr. Build. Mater. 290 (2021) 123144. https://doi.org/10.1016/j.conbuildmat.2021.123144.

[25] Q.H. Do, S. Bishnoi, K.L. Scrivener, Microstructural Modeling of Early-Age Creep in Hydrating Cement Paste, J. Eng. Mech. 142 (2016) 04016086. https://doi.org/10.1061/(asce)em.1943-7889.0001144.

[26] A.B. Giorla, C.F. Dunant, Microstructural effects in the simulation of creep of concrete, Cem. Concr. Res. 105 (2018) 44–53. https://doi.org/10.1016/j.cemconres.2017.12.001.

[27] E. Schlangen, E.J. Garboczi, Fracture simulations of concrete using lattice models: Computational aspects, Eng. Fract. Mech. 57 (1997) 319–332. https://doi.org/10.1016/S0013-7944(97)00010-6.

[28] E. Schlangen, J.G.M. van Mier, Simple lattice model for numerical simulation of fracture of concrete materials and structures, Mater. Struct. 25 (1992) 534–542. https://doi.org/10.1007/BF02472449.

[29] H. Zhang, Y. Xu, Y. Gan, Z. Chang, E. Schlangen, B. Šavija, Combined experimental and numerical study of uniaxial compression failure of hardened cement paste at micrometre length scale, Cem. Concr. Res. 126 (2019) 105925. https://doi.org/10.1016/J.CEMCONRES.2019.105925.
[30] B. Šavija, H. Zhang, E. Schlangen, Micromechanical testing and modelling of blast furnace slag cement pastes, Constr. Build. Mater. 239 (2020). https://doi.org/10.1016/j.conbuildmat.2019.117841.
[31] Y. Gan, H. Zhang, M. Liang, Y. Zhang, E. Schlangen, K. van Breugel, B. Šavija, Flexural strength and fatigue properties of interfacial transition zone at the microscale, Cem. Concr. Compos. 133 (2022) 104717. https://doi.org/10.1016/j.cemconcomp.2022.104717.
[32] Y. Gan, H. Zhang, M. Liang, E. Schlangen, K. van Breugel, B. Šavija, A numerical study of fatigue of hardened cement paste at the microscale, Int. J. Fatigue 151 (2021) 106401. https://doi.org/10.1016/J.IJFATIGUE.2021.106401.
[33] B. Chen, X. Wang, H. Zhou, S. Jiang, Y. Weng, Uncertainty propagation in reinforcement bond performance of 3D-printed concrete via generative-augmented ensemble learning, Structures 87 (2026) 111577. https://doi.org/10.1016/j.istruc.2026.111577.
[34] Y. Gan, M. Vandamme, H. Zhang, Y. Chen, E. Schlangen, K. van Breugel, B. Šavija, Micro-cantilever testing on the short-term creep behaviour of cement paste at micro-scale, Cem. Concr. Res. 134 (2020). https://doi.org/10.1016/j.cemconres.2020.106105.
[35] Y. Gan, M. Vandamme, Y. Chen, E. Schlangen, K. Van Breugel, B. Šavija, Experimental investigation of the short-term creep recovery of hardened cement paste at micrometre length scale, Cem. Concr. Res. 149 (2021) 106562. https://doi.org/10.1016/j.cemconres.2021.106562.
[36] Y. Gan, C.R. Rodriguez, E. Schlangen, K. Van Breugel, B. Šavija, Assessing strain rate sensitivity of cement paste at the micro-scale through micro-cantilever testing, Cem. Concr. Compos. 121 (2021) 104084. https://doi.org/10.1016/j.cemconcomp.2021.104084.
[37] Y. Gan, C. Romero Rodriguez, H. Zhang, E. Schlangen, K. van Breugel, B. Šavija, Modeling of microstructural effects on the creep of hardened cement paste using an experimentally informed lattice model, Comput.-Aided Civ. Infrastruct. Eng. 36 (2021) 560–576. https://doi.org/10.1111/mice.12659.
[38] Z. Chang, M. Liang, S. He, E. Schlangen, B. Šavija, Lattice modelling of early-age creep of 3D printed segments with the consideration of stress history, Mater. Des. 234 (2023) 112340. https://doi.org/10.1016/j.matdes.2023.112340.
[39] G. Di Luzio, L. Cedolin, C. Beltrami, Tridimensional Long-Term Finite Element Analysis of Reinforced Concrete Structures with Rate-Type Creep Approach, Appl. Sci. 10 (2020) 4772. https://doi.org/10.3390/app10144772.
[40] Y. Gan, H. Zhang, B. Šavija, E. Schlangen, K. Van Breugel, Static and Fatigue Tests on Cementitious Cantilever Beams Using Nanoindenter, Micromachines 9 (2018) 630. https://doi.org/10.3390/mi9120630.
[41] Qiang Yu, Zdenek P. Bazant, Roman Wendner, Improved Algorithm for Efficient and Realistic Creep Analysis of Large Creep-Sensitive Concrete Structures, ACI Struct. J. 109 (2012). https://doi.org/10.14359/51684044.
[42] Z.P. Bazant, S.T. Wu, Rate-type creep law of aging concrete based on Maxwell chain ER(t, r), (1974).
[43] M. Shahidi, B. Pichler, Ch. Hellmich, Interfacial Micromechanics Assessment of Classical Rheological Models. II: Multiple Interface Sizes and Viscosities, J. Eng.

Mech. 142 (2016) 04015093. https://doi.org/10.1061/(ASCE)EM.1943-7889.0001013.
[44] M. Shahidi, B. Pichler, Ch. Hellmich, Viscous interfaces as source for material creep: A continuum micromechanics approach, Eur. J. Mech. - ASolids 45 (2014) 41–58. https://doi.org/10.1016/j.euromechsol.2013.11.001.
[45] Z.P. Bažant, M. Jirásek, Creep and Hygrothermal Effects in Concrete Structures, Springer Netherlands, Dordrecht, 2018. https://doi.org/10.1007/978-94-024-1138-6.
[46] J. Mazars, A description of micro- and macroscale damage of concrete structures, Eng. Fract. Mech. 25 (1986) 729–737. https://doi.org/10.1016/0013-7944(86)90036-6.
[47] G. Pijaudier-Cabot, J. Mazars, Damage Models for Concrete, in: Handb. Mater. Behav. Models, Elsevier, 2001: pp. 500–512. https://doi.org/10.1016/B978-012443341-0/50056-9.
[48] M.R.T. Arruda, J. Pacheco, L.M.S. Castro, E. Julio, A modified Mazars damage model with energy regularization, Eng. Fract. Mech. 259 (2022) 108129. https://doi.org/10.1016/j.engfracmech.2021.108129.
[49] International Federation for Structural Concrete (fib), Fib Model Code for Concrete Structures 2010, Ernst & Sohn, Wiley, Berlin, Germany, 2013.
[50] C. Mazzotti, M. Savoia, Nonlinear Creep Damage Model for Concrete under Uniaxial Compression, J. Eng. Mech. 129 (2003) 1065–1075. https://doi.org/10.1061/(ASCE)0733-9399(2003)129:9(1065).
[51] R. Díaz Flores, C. Hellmich, B. Pichler, Nonlinear creep of concrete: Stress-activated stick–slip transition of viscous interfaces and microcracking-induced damage, Cem. Concr. Res. 191 (2025) 107809. https://doi.org/10.1016/j.cemconres.2025.107809.
[52] B. Hedegaard, Creep and Shrinkage Modeling of Concrete Using Solidification Theory, J. Mater. Civ. Eng. 32 (2020) 04020179. https://doi.org/10.1061/(asce)mt.1943-5533.0003256.
[53] H.S. Wong, M.K. Head, N.R. Buenfeld, Pore segmentation of cement-based materials from backscattered electron images, Cem. Concr. Res. 36 (2006) 1083–1090. https://doi.org/10.1016/j.cemconres.2005.10.006.
[54] M. Zhang, Y. He, G. Ye, D.A. Lange, K.V. Breugel, Computational investigation on mass diffusivity in Portland cement paste based on X-ray computed microtomography (μCT) image, Constr. Build. Mater. 27 (2012) 472–481. https://doi.org/10.1016/j.conbuildmat.2011.07.017.
[55] G. Constantinides, F.J. Ulm, The effect of two types of C-S-H on the elasticity of cement-based materials: Results from nanoindentation and micromechanical modeling, Cem. Concr. Res. 34 (2004) 67–80. https://doi.org/10.1016/S0008-8846(03)00230-8.
[56] K. Scrivener, R. Snellings, B. Lothenbach, A practical guide to microstructural analysis of cementitious materials, n.d.
[57] P.D. Tennis, H.M. Jennings, A model for two types of calcium silicate hydrate in the microstructure of Portland cement pastes, Cem. Concr. Res. 30 (2000) 855–863. https://doi.org/10.1016/S0008-8846(00)00257-X.
[58] K. Van Breugel, Simulation of hydration and formation of structure in hardening cement-based materials, Delft University of Technology, 1993.
[59] M. Königsberger, C. Hellmich, B. Pichler, Densification of C-S-H is mainly driven by available precipitation space, as quantified through an analytical cement hydration model based on NMR data, Cem. Concr. Res. 88 (2016) 170–183.

https://doi.org/10.1016/j.cemconres.2016.04.006.
[60] A.M. Gajewicz-Jaromin, P.J. McDonald, A.C.A. Muller, K.L. Scrivener, Influence of curing temperature on cement paste microstructure measured by 1H NMR relaxometry, Cem. Concr. Res. 122 (2019) 147–156. https://doi.org/10.1016/j.cemconres.2019.05.002.
[61] N. Jiménez Segura, B.L.A. Pichler, C. Hellmich, Mix-, storage- and temperature-invariant precipitation characteristics in white cement paste, expressed through an NMR-based analytical model, Cem. Concr. Res. 172 (2023) 107237. https://doi.org/10.1016/j.cemconres.2023.107237.
[62] A.C.A. Muller, K.L. Scrivener, A.M. Gajewicz, P.J. McDonald, Densification of C–S–H Measured by^{1} H NMR Relaxometry, J. Phys. Chem. C 117 (2013) 403–412. https://doi.org/10.1021/jp3102964.
[63] M. Liang, S. He, Y. Gan, H. Zhang, Z. Chang, E. Schlangen, B. Šavija, Predicting micromechanical properties of cement paste from backscattered electron (BSE) images by computer vision, Mater. Des. 229 (2023) 111905. https://doi.org/10.1016/j.matdes.2023.111905.
[64] X. Chen, D. Hou, Y. Han, X. Ding, P. Hua, Clustering analysis of grid nanoindentation data for cementitious materials, J. Mater. Sci. 56 (2021) 12238–12255. https://doi.org/10.1007/s10853-021-05848-8.
[65] C. Hu, Z. Li, A review on the mechanical properties of cement-based materials measured by nanoindentation, Constr. Build. Mater. 90 (2015) 80–90. https://doi.org/10.1016/j.conbuildmat.2015.05.008.
[66] F.J. Ulm, M. Vandamme, H.M. Jennings, J. Vanzo, M. Bentivegna, K.J. Krakowiak, G. Constantinides, C.P. Bobko, K.J. Van Vliet, Does microstructure matter for statistical nanoindentation techniques?, Cem. Concr. Compos. 32 (2010) 92–99. https://doi.org/10.1016/J.CEMCONCOMP.2009.08.007.
[67] L. Brown, P.G. Allison, F. Sanchez, Use of nanoindentation phase characterization and homogenization to estimate the elastic modulus of heterogeneously decalcified cement pastes, Mater. Des. 142 (2018) 308–318. https://doi.org/10.1016/J.MATDES.2018.01.030.
[68] S.-Y. Kim, D. Eum, H. Lee, K. Park, K. Terada, T.-S. Han, Evaluating tensile strength of cement paste using multiscale modeling and in-situ splitting tests with micro-CT, Constr. Build. Mater. 411 (2024) 134642. https://doi.org/10.1016/j.conbuildmat.2023.134642.
[69] T.-S. Han, D. Eum, S.-Y. Kim, J.-S. Kim, J.-H. Lim, K. Park, D. Stephan, Multi-scale analysis framework for predicting tensile strength of cement paste by combining experiments and simulations, Cem. Concr. Compos. 139 (2023) 105006. https://doi.org/10.1016/j.cemconcomp.2023.105006.
[70] Z. Zhang, Y. Yan, Z. Qu, G. Geng, Endowing strength to calcium silicate hydrate (C-S-H) powder by high pressure mechanical compaction, Cem. Concr. Res. 159 (2022) 106858. https://doi.org/10.1016/j.cemconres.2022.106858.
[71] H. Zhang, B. Šavija, M. Luković, E. Schlangen, Experimentally informed micromechanical modelling of cement paste: An approach coupling X-ray computed tomography and statistical nanoindentation, Compos. Part B Eng. 157 (2019) 109–122. https://doi.org/10.1016/j.compositesb.2018.08.102.
[72] G. Constantinides, F.-J. Ulm, The nanogranular nature of C–S–H, J. Mech. Phys. Solids 55 (2007) 64–90. https://doi.org/10.1016/j.jmps.2006.06.003.
[73] M. Hlobil, V. Šmilauer, G. Chanvillard, Micromechanical multiscale fracture model for compressive strength of blended cement pastes, Cem. Concr. Res. 83 (2016) 188–202. https://doi.org/10.1016/j.cemconres.2015.12.003.

[74] X. Cao, Y. Pan, C. Zhang, Y. Bi, H. Zhao, C. Yu, F. Yin, Molecular dynamics study on microporous direction effect on C-S-H fracture performance, Mater. Today Commun. 39 (2024) 109168. https://doi.org/10.1016/j.mtcomm.2024.109168.

[75] D. Fan, S. Yang, Mechanical properties of C-S-H globules and interfaces by molecular dynamics simulation, Constr. Build. Mater. 176 (2018) 573–582. https://doi.org/10.1016/j.conbuildmat.2018.05.085.

[76] M. Gupta, S. Bhowmik, Fracture insights on notched calcium silicate hydrate (C-S-H) and silica interface in concrete using reactive molecular dynamics simulations, Constr. Build. Mater. 499 (2025) 144081. https://doi.org/10.1016/j.conbuildmat.2025.144081.

[77] Z.P. Bazant, E. Osman, Double power law for basic creep of concrete, Matér. Constr. 9 (1976) 3–11.

[78] C. Pichler, R. Lackner, Upscaling of viscoelastic properties of highly-filled composites: Investigation of matrix–inclusion-type morphologies with power-law viscoelastic material response, Compos. Sci. Technol. 69 (2009) 2410–2420. https://doi.org/10.1016/J.COMPSCITECH.2009.06.008.

[79] I. Carol, Z.P. Bažant, Viscoelasticity with Aging Caused by Solidification of Nonaging Constituent, J. Eng. Mech. 119 (1993) 2252–2269. https://doi.org/10.1061/(ASCE)0733-9399(1993)119:11(2252).

[80] Z.P. Bažant, Y. Xi, Continuous Retardation Spectrum for Solidification Theory of Concrete Creep, J. Eng. Mech. 121 (1995) 281–288. https://doi.org/10.1061/(ASCE)0733-9399(1995)121:2(281).

[81] P. Virtanen, R. Gommers, T.E. Oliphant, M. Haberland, T. Reddy, D. Cournapeau, E. Burovski, P. Peterson, W. Weckesser, J. Bright, S.J. van der Walt, M. Brett, J. Wilson, K.J. Millman, N. Mayorov, A.R.J. Nelson, E. Jones, R. Kern, E. Larson, C.J. Carey, İ. Polat, Y. Feng, E.W. Moore, J. VanderPlas, D. Laxalde, J. Perktold, R. Cimrman, I. Henriksen, E.A. Quintero, C.R. Harris, A.M. Archibald, A.H. Ribeiro, F. Pedregosa, P. van Mulbregt, A. Vijaykumar, A.P. Bardelli, A. Rothberg, A. Hilboll, A. Kloeckner, A. Scopatz, A. Lee, A. Rokem, C.N. Woods, C. Fulton, C. Masson, C. Häggström, C. Fitzgerald, D.A. Nicholson, D.R. Hagen, D.V. Pasechnik, E. Olivetti, E. Martin, E. Wieser, F. Silva, F. Lenders, F. Wilhelm, G. Young, G.A. Price, G.-L. Ingold, G.E. Allen, G.R. Lee, H. Audren, I. Probst, J.P. Dietrich, J. Silterra, J.T. Webber, J. Slavič, J. Nothman, J. Buchner, J. Kulick, J.L. Schönberger, J.V. de Miranda Cardoso, J. Reimer, J. Harrington, J.L.C. Rodríguez, J. Nunez-Iglesias, J. Kuczynski, K. Tritz, M. Thoma, M. Newville, M. Kümmerer, M. Bolingbroke, M. Tartre, M. Pak, N.J. Smith, N. Nowaczyk, N. Shebanov, O. Pavlyk, P.A. Brodtkorb, P. Lee, R.T. McGibbon, R. Feldbauer, S. Lewis, S. Tygier, S. Sievert, S. Vigna, S. Peterson, S. More, T. Pudlik, T. Oshima, T.J. Pingel, T.P. Robitaille, T. Spura, T.R. Jones, T. Cera, T. Leslie, T. Zito, T. Krauss, U. Upadhyay, Y.O. Halchenko, Y. Vázquez-Baeza, SciPy 1.0: fundamental algorithms for scientific computing in Python, Nat. Methods 17 (2020) 261–272. https://doi.org/10.1038/s41592-019-0686-2.

[82] M. Vandamme, The Nanogranular Origin of Concrete Creep: A Nanoindentation Investigation of Microstructure and Fundamental Properties of Calcium-Silicate-Hydrates, Massachusetts Institute of Technology, 2002.

[83] S. Mallick, M.B. Anoop, K.B. Rao, Creep of cement paste containing fly ash - An investigation using microindentation technique, Cem. Concr. Res. 121 (2019) 21–36. https://doi.org/10.1016/j.cemconres.2019.04.006.

[84] M. Sorgner, R. Díaz Flores, B. Pichler, T. Pilgerstorfer, B. Moritz, C. Hellmich,

Basic creep properties of hydrates in mature slag-based CEM II concretes: A micromechanical analysis, Cem. Concr. Res. 189 (2025) 107735. https://doi.org/10.1016/j.cemconres.2024.107735.
[85] M. Irfan-ul-Hassan, B. Pichler, R. Reihsner, Ch. Hellmich, Elastic and creep properties of young cement paste, as determined from hourly repeated minute-long quasi-static tests, Cem. Concr. Res. 82 (2016) 36–49. https://doi.org/10.1016/j.cemconres.2015.11.007.
[86] E. Binder, M. Königsberger, R. Díaz Flores, H.A. Mang, C. Hellmich, B.L.A. Pichler, Thermally activated viscoelasticity of cement paste: Minute-long creep tests and micromechanical link to molecular properties, Cem. Concr. Res. 163 (2023) 107014. https://doi.org/10.1016/j.cemconres.2022.107014.
[87] W. Guo, Y. Wei, Investigation of compressive creep of calcium-silicate-hydrates (C-S-H) in hardened cement paste through micropillar testing, Cem. Concr. Res. 177 (2024) 107427. https://doi.org/10.1016/j.cemconres.2024.107427.
[88] T.-S. Han, X. Zhang, J.-S. Kim, S.-Y. Chung, J.-H. Lim, C. Linder, Area of lineal-path function for describing the pore microstructures of cement paste and their relations to the mechanical properties simulated from μ-CT microstructures, Cem. Concr. Compos. 89 (2018) 1–17. https://doi.org/10.1016/j.cemconcomp.2018.02.008.
[89] R. Blanchard, A. Dejaco, E. Bongaers, C. Hellmich, Intravoxel bone micromechanics for microCT-based finite element simulations, J. Biomech. 46 (2013) 2710–2721. https://doi.org/10.1016/j.jbiomech.2013.06.036.
[90] M. Liang, Y. Fang, W. Guo, C. He, E. Schlangen, B. Šavija, S. Contera, Deep active sequential learning of stress evolution in early-age concrete informed by thermo-chemo-mechanical modelling, Eng. Appl. Artif. Intell. 177 (2026) 114985. https://doi.org/10.1016/j.engappai.2026.114985.
[91] M. Liang, G.D. Luzio, E. Schlangen, B. Šavija, Experimentally informed modeling of the early-age stress evolution in cementitious materials using exponential conversion from creep to relaxation, Comput.-Aided Civ. Infrastruct. Eng. 39 (2024) 3507–3530. https://doi.org/10.1111/mice.13156.
[92] M. Liang, Z. Li, S. He, Z. Chang, Y. Gan, E. Schlangen, B. Šavija, Stress evolution in restrained GGBFS concrete due to autogenous deformation: bayesian optimization of aging creep, Constr. Build. Mater. 324 (2022) 126690. https://doi.org/10.1016/J.CONBUILDMAT.2022.126690.
[93] Z. Hu, M. Wyrzykowski, M. Griffa, K. Scrivener, P. Lura, Young's modulus and creep of calcium-silicate-hydrate compacts measured by microindentation, Cem. Concr. Res. 134 (2020). https://doi.org/10.1016/j.cemconres.2020.106104.
[94] J.J. Chen, L. Sorelli, M. Vandamme, F. Ulm, G. Chanvillard, A Coupled Nanoindentation/SEM-EDS Study on Low Water/Cement Ratio Portland Cement Paste: Evidence for C–S–H/$Ca(OH)_2$ Nanocomposites, J. Am. Ceram. Soc. 93 (2010) 1484–1493. https://doi.org/10.1111/j.1551-2916.2009.03599.x.
[95] C. Liu, Z. Chen, Q. Lv, M. Liang, Y. Zhang, Multiscale pore structure segmentation of cementitious materials using light-weight and modified VGG-Unet network, J. Build. Eng. 111 (2025) 113618. https://doi.org/10.1016/j.jobe.2025.113618.
[96] I. Fischer, B. Pichler, E. Lach, C. Terner, E. Barraud, F. Britz, Compressive strength of cement paste as a function of loading rate: Experiments and engineering mechanics analysis, Cem. Concr. Res. 58 (2014) 186–200. https://doi.org/10.1016/j.cemconres.2014.01.013.